Journal of Materials Chemistry A

REVIEW

View Article Online
View Journal | View Issue

Cite this: J. Mater. Chem. A, 2023, 11, 23106

The metal–support interaction effect in the carbon-free PEMFC cathode catalysts

Feilong Dong, Yarong Liu, Zunhang Lv, Changli Wang, Wenxiu Yang * and Bo Wang *

Proton exchange membrane fuel cells (PEMFCs) have been regarded as an effective means to transform hydrogen energy into electric energy, which is featured with high energy density, excellent conversion efficiency, and environmental friendliness. Carbon nanomaterials are the most widely used supports for the state-of-the-art Pt-based PEMFC cathode catalysts. Nonetheless, the corrosion of carbon supports under high potential environment would inevitably lead to the dissolution/ripening of Pt, resulting in the severe degradation of their PEMFC performance. Carbon-free materials, such as transition metal oxides/nitrides/sulfides/carbides (TMOs, TMNs, TMSs, and TMCs), can effectively prevent this issue with their excellent intrinsic stability and tuned metal–support interactions (MSI). Recently, numerous researches have been focused on the design and preparation of carbon-free PEMFC cathode catalysts. Meanwhile, MSI effect, including d-band center, migration energy barrier, defect sites, coordination environment, and electron transfer ability, have also been considered to improve the PEMFCs performance. In this review, the MSI effect of carbon-free PEMFC cathode materials and their common adjustment strategies are systematically summarized. Then, details about the pristine and modified carbon-free PEMFC catalysts and their specific structure–activity relationships induced by MSI effect are further illustrated in the order of TMOs, TMCs, TMNs, and TMSs. Finally, the challenges and perspectives of carbon-free PEMFC cathode catalysts are further proposed to provide insights into future researches in this PEMFC field.

Received 10th August 2023
Accepted 29th August 2023

DOI: 10.1039/d3ta04792j

rsc.li/materials-a

1 Introduction

Recently, environmental problems, such as global warming and air pollution, caused by the excessive use of fossil energy have become one of the greatest global challenges. In order to promote the worldwide zero carbon emission, it is urgent to develop eco-friendly and sustainable new energy system. Hydrogen energy, as a secondary energy source, is characterized by high combustion calorific value, abundant resources, and

Key Laboratory of Cluster Science Ministry of Education, Beijing Key Laboratory of Photoelectronic/Electrophotonic Conversion Materials, Advanced Technology Research Institute (Jinan), Advanced Research Institute of Multidisciplinary Science, School of Chemistry and Chemical Engineering, Beijing Institute of Technology, Beijing 100081, China. E-mail: yangwx19@bit.edu.cn; bowang@bit.edu.cn

Feilong Dong received her B.S. degree from Ningxia University in 2022. She is now pursuing her M.S. degree under the supervision of Prof. Wenxiu Yang and Prof. Bo Wang at the School of Chemistry and Chemical Engineering, Beijing Institute of Technology. Her research interests include the design and synthesis of novel functional porous nanomaterials for PEM fuel cell.

Yarong Liu received her M.S. degree from Zhengzhou University in 2020. She is now pursuing her PhD degree under the supervision of Prof. Wenxiu Yang and Prof. Bo Wang at the School of Chemistry and Chemical Engineering, Beijing Institute of Technology. Her research interests include the design and synthesis of metal–organic frameworks and their derived nanocarbon materials for PEM fuel cell and metal–air batteries.

cleanliness, which can alleviate the shortage of fossil energy and environmental problems. Proton exchange membrane fuel cells (PEMFCs) are effective devices in utilizing the hydrogen energy, which can accomplish the transformation of chemical energy into electric energy.[1,2] In addition, it is featured with high energy density, excellent conversion efficiency, environmental friendliness, and starts quickly at low temperature. Owing to these advantages, PEMFCs have shown important application potential in the past decades.[3–5]

Oxygen reduction reaction (ORR) is the key step in PEMFCs; however, it suffers from sluggish kinetics. Currently, Pt-based nanocrystals-anchored carbon composites (Pt/C) are the state-of-the-art ORR catalysts, where regulatory strategies for geometric and electronic structure have been accordingly provided to achieve the most active Pt/C catalysts for PEMFCs. However, under the strong oxidative/acidic conditions of PEMFCs, severe deactivation issues still exist for commercial Pt/C catalysts (>55% mass activity (MA) loss after 30 000 voltage cycles), which is far from the target of U.S. DOE 2025 (after 30 000 voltage cycles, MA loss is less than 40%).[6–9] Details for this deactivation mechanism of Pt/C are as follows: (1) the insufficient metal–support interaction; (2) the corrosion of the carbon carriers; (3) the dissolution, migration and redeposition of the precious metals. Moreover, the local cathode potential will be as high as 1.5 V (*vs.* reversible hydrogen electrode (RHE)) under the circumstances of fuel cell start-stop or load-changing, further causing the rapid oxidation of the carbon support.[10,11] As proved by the reported results, this oxidation process can lead to the compaction or collapse of nanopores near the surface (less than 100 nm in size). Concretely, the total porosity and surface area of these oxidized carbon carriers will be respectively lost by ~35% and ~13% after 1000 start-stop cycles of PEMFCs,[12] which results in the agglomeration of metal active sites and the reduction of PEMFCs lifetime.[13] Hence, it is essential to develop efficient supports for PEMFC cathode catalysts with improved long-time tolerance and metal–support interaction, ultimately boosting the commercialization of PEMFCs. Recently, researches have mainly solved this issue from two approaches, including optimizing the poor-stability of carbon and exploring novel carbon-free supports. The details are as follows.

As for the optimized stability of carbon-based carriers, enhancing the carbon graphitization degree and decreasing the exposed carbon edge defects have been verified as efficient methods to achieve this goal.[14,15] With the increase in carbon

Zunhang Lv received his B.S. degree from Qufu Normal University in 2014 and M.S. degree in 2018 from Qingdao University of Science and Technology. He is now pursuing his PhD degree under the supervision of Prof. Wenxiu Yang and Prof. Bo Wang at the School of Chemistry and Chemical Engineering, Beijing Institute of Technology. His research interests focus on the design and synthesis of functional nanomaterials for electrocatalysis.

Wenxiu Yang received her B.S. degree from Lanzhou University in 2012 and PhD degree in analytical chemistry in 2017 from the Changchun Institute of Applied Chemistry, Chinese Academy of Sciences. After a postdoctoral fellowship at Peking University, she is now an Associate Professor at the Beijing Institute of Technology. Her research mainly focuses on the synthesis and surface/interface modification of functional nanomaterials and their applications in electrocatalysis (e.g., ORR, HER, OER, and CO_2RR) and energy storage (e.g., PEMFC, zinc–air batteries, and PEMEC).

Changli Wang received his B.S. degree from Yangzhou University in 2021. He is now pursuing his M.S. degree under the supervision of Prof. Wenxiu Yang and Prof. Bo Wang at the School of Chemistry and Chemical Engineering, Beijing Institute of Technology. His research interests include the design and synthesis of functional porous frameworks for electrocatalytic CO_2 reduction reaction.

Bo Wang obtained his B.S. and M.S. degrees from Peking University in 2004 and the University of Michigan in 2006, respectively, and his PhD from the University of California Los Angeles in 2008. He has been a professor in the School of Chemistry and Chemical Engineering, Beijing Institute of Technology since 2011. His research interests are the design and synthesis of novel functional porous frameworks, energy storage, advanced battery materials, gas purification, toxicant capture, and sensing.

graphitization, carbon nanomaterials such as graphene, carbon nanotubes, and other *in situ* formed graphitized carbon frameworks can show improved ORR stability.[16,17] Meanwhile, carbon carriers with flat surface exhibit better durability than that with abundant edge defects. Also, the negative effect on the durability induced by hydrogen-groups-rich edges such as C–H, C–OH, and C–COOH is severer compared to the ether ring groups.[18] Despite the negative impact of defects on the stability of carbon-based ORR catalysts, many reports have also confirmed that carbon defects can optimize the electron structure of metal active sites and synergistically enhance the ORR performance.[19] For example, designing defect-rich M-N_4-carbon catalysts could change the microscopic coordination environment of active sites, thus optimizing the adsorption of ORR intermediates and increasing their ORR activities.[20,21] Therefore, simultaneously improving the activity and stability of carbon-based ORR catalysts remains a huge challenge in the field of carbon-based ORR catalysts.

Besides, as for the novel carbon-free supports, transition metal-based nanomaterials (named as TMXs) have attracted much attention in recent years for PEMFC cathodes, for example, transition metal oxides (TMOs), transition metal carbide (TMCs), transition metal nitrides (TMNs), and transition metal sulfide (TMSs). Compared with carbon supports, most of these carbon-free supports have excellent chemical/electrochemical stability and MSI under the PEMFCs conditions, yet some of them still suffer from low conductivity and insufficient anchoring sites. In view of these problems, adjusting the geometric structure has been used to tune their specific surface area, pore distribution, and exposed anchor sites, offering huge possibility for developing stable and active PEMFC cathode catalysts. In addition, strategies such as heterometal atoms doping, metal-free heteroatoms doping (S, N, P, *etc.*), coating engineering, and partial oxidizing/sulfurizing have also been provided to facilitate their MSI effect. Meanwhile, with the aid of advanced nanocharacterization/theoretical calculation techniques, the MSI effect of these carbon-free ORR catalysts can be further analyzed, ultimately prompting the in-depth understanding of structure–activity relationships.

So far, a majority of the reviews on PEMFC cathode catalysts are focused on novel carbon-supported nanocatalysts, including, Pt-based alloys,[22,23] platinum group metal (PGM)-free catalysts,[24–26] metal–organic frameworks based catalysts,[27] single atom catalyst (SCAs),[28–31] diatomic metals,[32] and nanocarbon catalysts.[33–35] Few reviews can provide a comprehensive summary on carbon-free PEMFC cathode catalysts, especially those that can logically analyze the MSI effect and structure–activity relationships. Therefore, it is necessary to illustrate the relevant researches, which can prompt the accurate design of non-carbon-based PEMFC cathode ORR electrocatalysts and the deep understanding of reaction mechanisms. In this paper, the MSI effect of the carbon-free PEMFC cathode materials and common adjustment strategies are systematically illustrated (Fig. 1). Then, several pristine and modified non-carbon ORR catalysts are further illustrated in the order TMOs, TMCs, TMNs, TMSs, *etc.* so as to better analyze the MSI effect-induced structure–activity relationships of these catalysts. Last but not least, the challenges and prospectives of non-carbon cathode catalysts for PEMFCs are prospected based on the latest research progress, aiming to boost the development and widespread application of PEMFCs device.

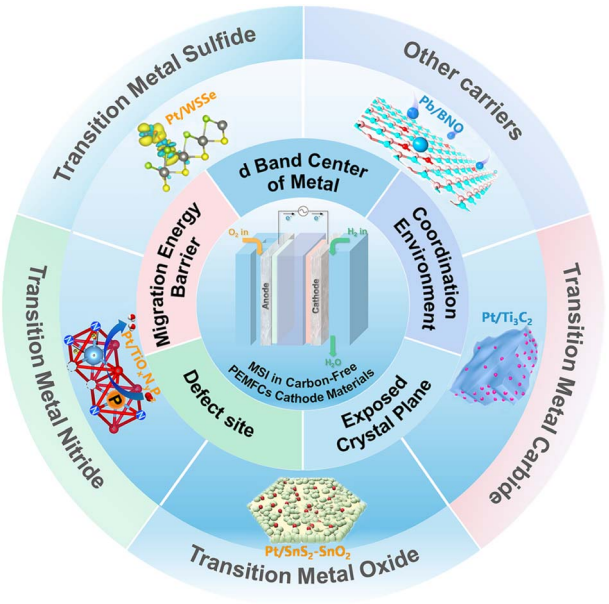

Fig. 1 The regulation strategies for the MSI effect and common types of carbon-free carriers in PEMFC cathodes.

2 Regulation mechanism of MSI in carbon-free ORR catalyst for PEMFCs

Supported metal catalysts, where active metal species are anchored on the surface of nanocarriers, have been widely used in the energy storage and conversion process,[36–38] especially in PEMFCs.[39,40] In general, excellent supports can improve the dispersion and utilization efficiency of metal active species, and some of them can even participate in these electrochemical processes.[41,42] According to their roles, supports can be divided into inert and active nanomaterials.[43] For example, nanomaterials including nanocarbon, silicon oxide, and alumina are regarded as inert supports. Due to the lack of reducibility of such materials, it is difficult to release reactive oxygen species under the practical electrochemical conditions, ultimately showing inertia toward the catalytic reaction. On the contrary, the active supports are mainly referred to as reducible MXs, such as reducible metal oxides, metal carbides, metal nitrides, and metal sulfides. Meanwhile, chemical bonds and strong MSI can be detected at the interfaces between these reducible MXs supports and metal active sites,[44] which will facilitate their enhanced catalytic activity, selectivity, and stability.

As for PEMFC cathode catalysts, the positive effect of MSI in MXs-supported M* (M* = transition metal active site)-based catalysts (MXs-M*) can be illustrated as follows: (a) reducing the d band center of metal. The M–M* bond formed in MXs-M* can promote the electron transfer from the carrier to the active metal species through electronic MSI, thus reducing the d-band

center and oxygen adsorption energy of the M* sites and ultimately improving their ORR performance;[45–47] (b) optimizing the coordination environment of M*. The presence of X in MXs can not only provide anchor sites for M* but also optimize the coordination environment of M*, leading to an enhanced the ORR activity. Moreover, the formation of the M*–X bond (X = O, N, S, C) in MXs-M* can improve the migration barrier of these carrier surface and prevent the aggregation of active metal species through the strong MSI effect;[48] (c) adjusting the exposed crystal plane. The exposed crystal plane of M* can be effectively tuned by MXs so as to maximize the density of the active crystal plane for the ORR process;[49–51] (d) enhancing the migration energy barrier. The MXs carriers can also be regarded as coating layers for M*, preventing their migration and aggregation during the ORR process. Also, many previous strategies such as mechanical-milling or chemical-etching have been further used to adjust the encapsulation degree and thickness of this coating layer, ultimately avoiding negative effect of the excessive encapsulation layer on the active M* sites and promoting the electron transfer property between the M* and adsorbed oxygen;[52,53] (e) forming the defect site. The vacancies, non-metal atom doping engineering, defect site, and heterojunction in the MXs carriers can be beneficial for the anchoring of the active metal species and the electron transfer within these composites.[54] Table 1 summarizes the RDE and PEMFC results of representative carbon-free catalysts, which are induced by different MSI effects.

3 Carbon-free carriers

3.1 Transition metal oxide carriers (TMOs)

Based on the Pourbaix diagram, TMOs have been demonstrated to be stable and possess great durability against oxidation reactions in harsh environments (pH < 1.0; 1.0–1.5 V),[55–57] which is owing to the high valence state of the metals in TMOs. Meanwhile, the M*–O bond in TMOs–M* can improve the migration barrier of M* and prevent the aggregation of M*. In addition, doping strategies and forming heterostructures are regarded as efficient methods to improve the electrical conductivity of TMOs. The above advantages of transition metal oxide carriers make it possible to be alternative catalyst supports in PEMFCs.

3.1.1 MSI effect between TMOs and M*. Since 1978, Tauster *et al.* have investigated that the chemisorption abilities of TiO_2-loaded noble metal composites toward small gas molecules, *e.g.*, CO and H_2. After a reduction treatment at 500 °C, the chemisorption abilities would suddenly disappear.[58] Based on the experimental results, they also found that the lowering of the sorption capacity was not due to the agglomeration of supported noble metals but caused by the changing of chemical interaction between the noble metal and the supports. In this case, the term "strong metal–support interaction (SMSI)" was proposed to describe this phenomenon.

After that, many researches have been focused on TMOs–M*, further exploring the origin of the SMSI effect. For example, it has been demonstrated that the work function of TMOs can be tuned by optimizing their oxygen vacancy concentration.[61] Therefore, a huge difference in the work function between TMOs and M* species (*e.g.*, Pt (5.84 eV)) can be achieved to enhance the charge transfer property in TMOs–M*, allowing more electrons to be injected into the d-band of the active metal species.[62–64] Moreover, a linear relationship can be summarized between the d-band center of M* and oxygen vacancy concentration of TMOs, verifying the key role of oxygen vacancy concentration for the adjustment of electronic MSI. Adhesion energy between TMOs and M* is another key descriptor for TMOs–M*, which have a significant effect on the sintering onset temperature of metals.[65] It has been reported that the higher adhesion energy and migration barrier of TMOs-supported composites catalysts can effectively prevent the agglomeration of the M* species. Beyond that, heteroatom doping, heterostructures, defects, *etc.*, can also be applied to optimize the SMSI effect of TMOs–M* and improve their catalytic activities for ORR. Detailed researches on the pristine and modified TMOs-supported catalysts are given below.

3.1.2 Pristine transition metal oxide carriers. To date, metal oxides such as WO_3, SnO_2, and CeO_2 have aroused infinite interests as alternative electrocatalyst supports for PEMFCs. As is known, some of TMOs still suffer from poor electrical conductivity. To make full use of the MSI effect and decrease the effect of low-conductivity, in the initial research, TMOs were always combined with carbon to produce TMOs–carbon composite supports for PEMFC cathode. For example, Dou *et al.* compounded Pt/WO_3/C nanocomposites by means of parallel WO_3 nanorods as PEMFC cathode catalysts. As revealed in TEM image, the average size of Pt nanoparticles (NPs) anchored to WO_3/C was 1.6 nm, which is quite smaller than that for Pt/C (*ca.* 2.4 nm). As a result, Pt/WO_3/C exhibited an enhanced electrochemical activity and stability for ORR compared with Pt/C.[66]

Li *et al.* developed a cable-like carbon nanotubes (CNTs) @SnO_2 core@shell structure supporting the Pt NPs, which exhibited high performance of ORR catalysis as advanced PEMFC cathode catalysts. Sn^{2+} precursor was predeterminedly nucleated at the carbonyl matrix and oxidized into SnO_2 on the surface of CNTs and grew up to completely cover its surface; immediately, Pt NPs were loaded onto the CNT@SnO_2 using the ethylene glycol reduction method (Fig. 2a and b). Density functional theory (DFT) calculations suggested that CNT@SnO_2 have higher adhesion energy and higher migration barrier for Pt atoms compared with conventional carbon carriers due to the SMSI between SnO_2 and Pt, preventing the Pt NPs from agglomeration (Fig. 2c). Meanwhile, the concentration of oxygen vacancy in SnO_2 could regulate the SMSI between SnO_2 and Pt NPs, which could properly reduce the d-band center of Pt (Fig. 2d) and optimize the ORR activity. The presence of a small amount of CNTs (~20 wt%) enhanced the conductivity of the carrier; meanwhile, SnO_2 on the CNTs surface can effectively prevent CNTs support from corrosion and collapse in the high-potential environment of PEMFCs. Impressively, the Pt-CNT@SnO_2 catalyst with optimal d-band center of Pt achieved the most excellent activity (MA = 0.68 A mg_{Pt}^{-1} under 0.9 V_{iR}-free, peak power density = 1618 mW cm^{-2}), and high stability in H_2–O_2 fuel cells after 5000 cycles under 1.0–1.5 V (MA loss =

Table 1 Summary of RDE and PEMFC measurement results for representative carbon-free catalysts induced by different MSI effects

			RDE performance			Fuel cell performance		
MSI effect between TMXs and M*	Representative catalyst	Electrolytes	$E_{1/2}$ (V)	Mass activity (mA mg_{Pt}^{-1})	Durability	P_{max} (mW cm^{-2})	Durability	Ref.
d Band center of metal	Pt/SnO_2@CNT	0.1 M $HClO_4$	0.887	680 at 0.9 V_{RHE}	MA loss 20.5% at 0.9 V (50 000 cycles) $E_{1/2}$ loss 11 mV (30 000 cycles) under 1.0–1.5 V $E_{1/2}$ loss of Pt-CNT 78 mV (30 000 cycles) under 1.0–1.5 V	1618	MA loss 9.2% (5000 cycles) P_{max} loss 8% (5000 cycles)	55
	FePc/GaS	0.1 M KOH	0.87	—	Current density loss negligibly (5000 cycles)	—	—	145
	Pt/TiNiN	0.1 M $HClO_4$	0.893	830 at 0.9 V_{RHE}	$E_{1/2}$ loss 10 mV (10 000 cycles) $E_{1/2}$ loss of Pt/C 25 mV (10 000 cycles)	—	—	131
	$Pt/Ti_{0.9}Co_{0.1}N$	0.1 M $HClO_4$	0.905	460 at 0.9 V_{RHE}	ECSA remaining 65% (10 000 cycles)	—	—	130
Exposed crystal plane	Pt/Sb–SnO_2	0.1 M $HClO_4$	—	102 at 0.9 V_{RHE}	ECSA remaining 100% (10 000 cycles) compared to 57.6% retention for Pt/C	478	P_{max} loss 8% (1000 cycles)	66
	Pt/TiN	0.1 M $HClO_4$	0.88	440 at 0.9 V_{RHE}	$E_{1/2}$ loss 19 mV (3000 cycles) under 0.6–1.2 V $E_{1/2}$ loss of Pt/C 144 mV (3000 cycles) under 0.6–1.2 V	—	—	122
Migration energy barrier	Pt/SnS_2–SnO_2	0.1 M $HClO_4$	0.895	400 at 0.9 V_{RHE}	MA loss 23.7% (50 000 cycles) under 1.0–1.6 V MA loss of Pt/C 96.2% (50 000 cycles) under 1.0–1.6 V	700	—	75
	Pt/Co_6Mo_6C NSs-G	0.1 M $HClO_4$	0.935	957 at 0.9 V_{RHE}	$E_{1/2}$ loss 9 mV (10 000 cycles) under 0.6–1.2 V $E_{1/2}$ loss of Pt/C 69 mV (10 000 cycles) under 0.6–1.2 V	—	—	99
	Pd/p-BNO	0.1 M KOH	0.89	253 at 0.9 V_{RHE}	$E_{1/2}$ loss 4 mV (5000 cycles) $E_{1/2}$ loss of Pt/C 15 mV (5000 cycles)	—	—	172
Defect site	WC/FeS/FePt/NC	0.1 M $HClO_4$	0.925	—	Current retention ~52.4% (18 000 s) at high potential of 0.8 V Pt/C is only 33.5%	—	—	158
	Pt–CeO_2-NC	0.1 M $HClO_4$	0.876	593.6 at 0.9 V_{RHE}	$E_{1/2}$ loss 5 mV (10 000 cycles) under 0.6–1.0 V $E_{1/2}$ loss of Pt/C 43 mV (10 000 cycles) under 0.6–1.0 V	—	—	56
	Pt/22L-Ti_3C_2	0.1 M $HClO_4$	—	40 at 0.9 V_{RHE}	Charge transfer current remaining 97% (5000 cycles)	~1200	No obvious decay of performance (30 000 cycles)	95
Coordination environment of M*	o-MQFe(FeN_3O–O–$Ti_3C_2O_x$)	0.1 M KOH	0.861	—	$E_{1/2}$ loss 16 mV (5000 cycles) $E_{1/2}$ loss of Pt/C 25 mV (5000 cycles) current remaining 88.3% (20 h) Current of Pt/C remaining 69.1% (20 h)	407.5	—	110
	$Co_3(HADQ)_2$	0.5 M H_2SO_4	0.836	—	Current density loss 5.4% at 0.85 V (20 000 cycles)	—	—	159

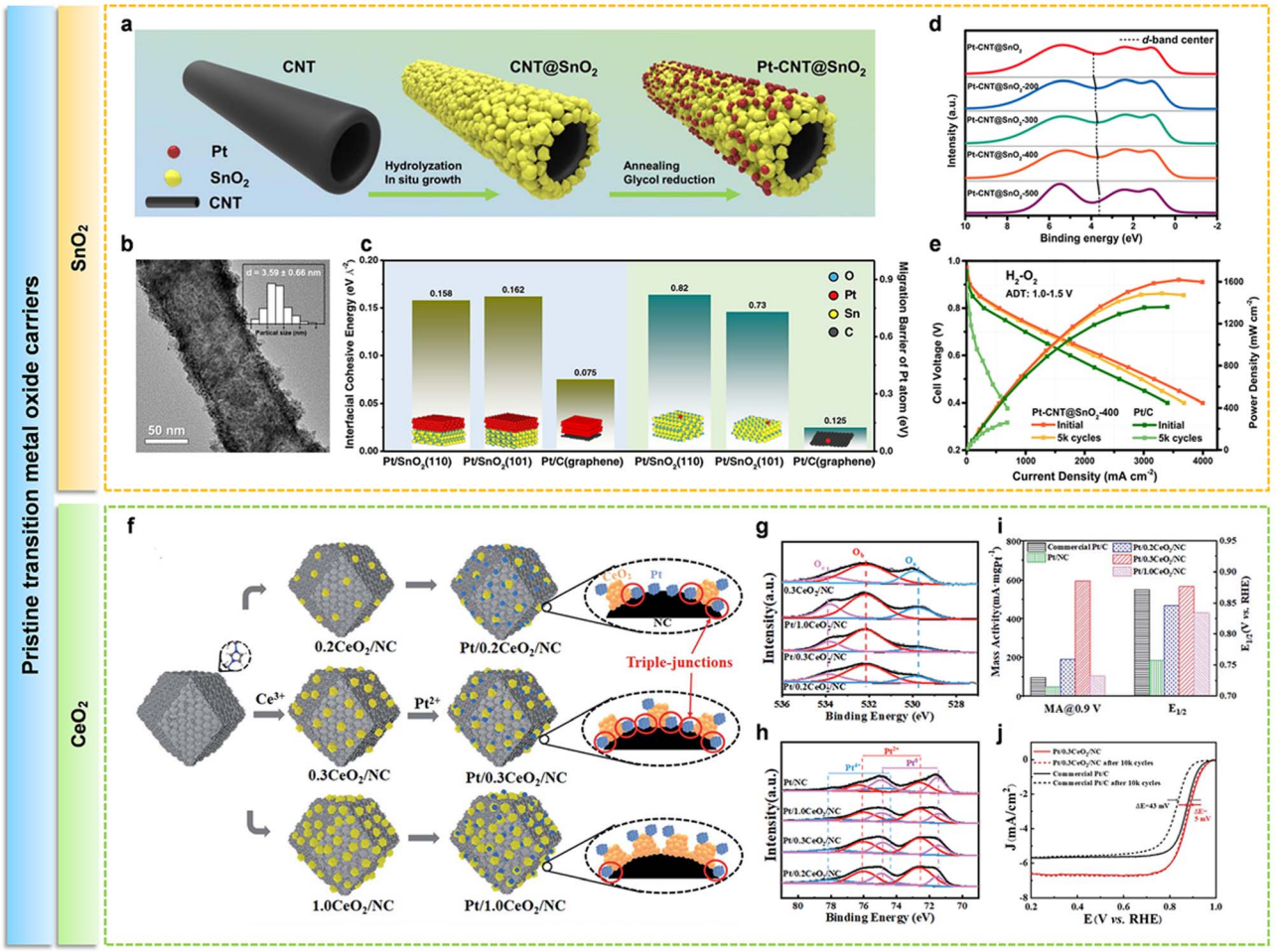

Fig. 2 (a) Scheme of the synthetic processes to Pt-CNT@SnO_2-T. (b) High resolution transmission electronmicroscopy (HRTEM) image of the Pt-CNT@SnO_2-400 (inset: statistical distribution of particle size). (c) The interfacial cohesive energies and energy barriers of a Pt atom migrating on the surfaces of Pt/SnO_2(110), Pt/SnO_2(101), and Pt/graphene, respectively. (d) Valence band XPS spectra of Pt-CNT@SnO_2 (black dotted line: the position of the d-band center). (e) H_2–O_2 fuel cell polarization curves of commercial Pt/C and Pt-CNT@SnO_2-400 after 5000 cycles under 1.0–1.5 V. Reproduced with permission.[59] Copyright 2022, Elsevier B.V. (f) Scheme of the synthesis route of Pt–CeO_2-NC catalysts. (g and h) High resolution XPS spectra of (g) O 1s and (h) Pt 4f. (i) MA at 0.9 V (*vs.* RHE) and half-wave potential of Pt–CeO_2–NC, Pt/NC, and commercial Pt/C. (j) LSV curves of commercial Pt/C and Pt–CeO_2–NC with optimal CeO_2 ratio before and after 10 000 cycles. Reproduced with permission.[60] Copyright 2022, The Royal Society of Chemistry.

9.2%, power density loss = 8%), compared with the previously reported Pt-based catalysts (Fig. 2e).[59] Numerous studies have focused on increasing the adhesion energy between metal NPs and supports so as to boost the stability of small metal particles during the operation of PEMFCs. By controlling the density of distributed CeO_2 nanocrystals on the NC support, Lu *et al.* successfully avoided the single contact between Pt and CeO_2 or the NC support and demonstrated a triple-junction interface of Pt–CeO_2–nitrogen-doped carbon (Pt–CeO_2-NC) (Fig. 2f). The Pt–CeO_2–NC CeO_2 nanocrystals included several oxygen vacancies. It can be seen from Fig. 2g that in the Pt–CeO_2–NC catalyst, the CeO_2 nanocrystals had a high concentration of oxygen vacancies and anchored Pt NPs tightly *via* the SMSI, which can alter the chemical state of Pt and prompt the electron transfer from NC support to Pt (Fig. 2h). The well-controlled Pt–CeO_2–NC triple-junction catalyst demonstrated exceptional activity and stability in acidic media with an MA of 593.6 mA mg_{Pt}^{-1} (6.1 times that of commercial Pt/C) (Fig. 2i) and a 5 mV decline of half-wave potential after 10 000 cycles of accelerated durability test (ADT) (Fig. 2j), which outperformed the results for Pt/CeO_2 catalysts that have been reported in previous investigations. The significance of Pt-oxide-support triple-junctions for developing extremely effective Pt electrocatalysts is highlighted by this work.[60]

Meanwhile, altering the oxide interfacial characteristics by means of concentrating defects, terminating surfaces, functionalizing surfaces, or changing reaction conditions can also be used to improve the ORR performance. Niu *et al.* prepared defect-rich Ti_4O_7 support by ball milling and sonication treatments to load Pd NPs. EPR and XPS indicated the SMSI and high conductivity induced by abundant oxygen vacancies and disorder layers in the treated Ti_4O_7 support, which are crucial for enhancing the ORR activity of Pd/Ti_4O_7.[69]

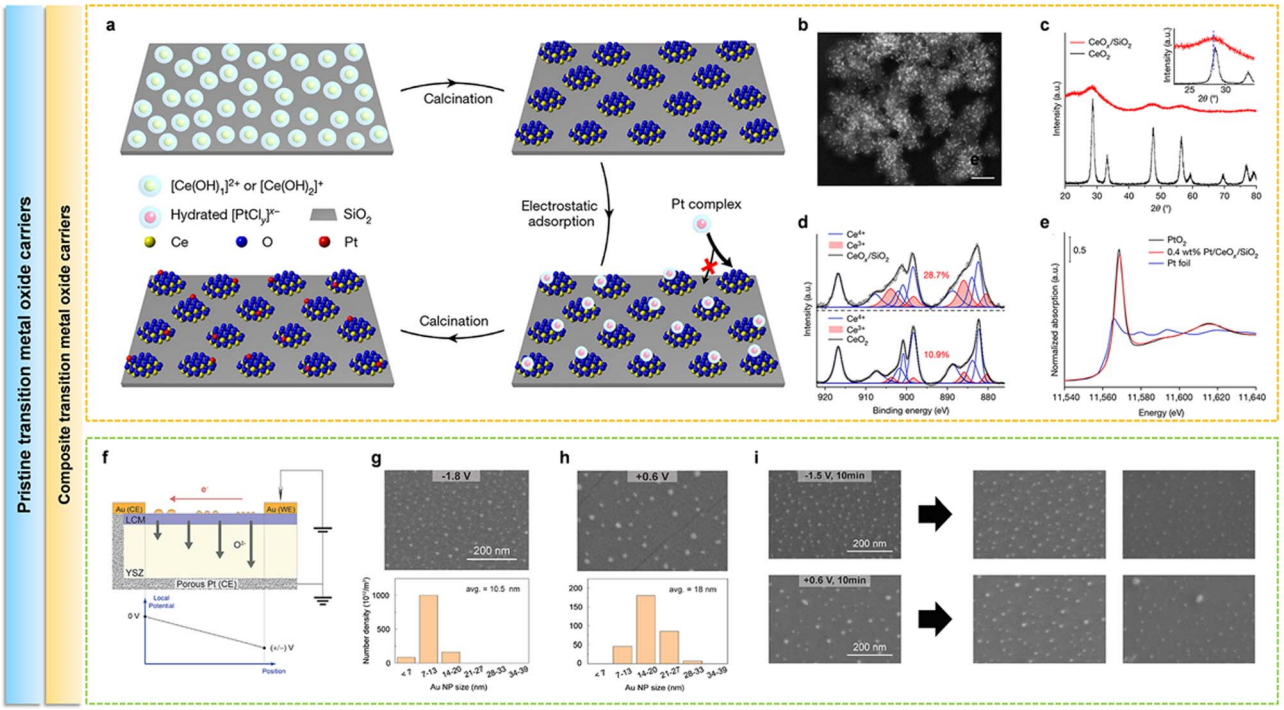

Fig. 3 (a) Schematic diagrams displaying the fabrication route of functional CeO_x nanoglue islands and CeO_x/SiO_2-supported Pt single-atom. (b) Low-magnification HAADF-STEM study of the conformally coated mesoporous, high-surface-area SiO_2 substrate with the as-prepared CeO_x nanoclusters. (c) Powder XRD patterns of CeO_x/SiO_2 and pure CeO_2 NPs. Inset: shows broadening and shifting of the peak position of CeO_x nanoclusters. (d) Ce 3d XPS data for SiO_2-supported CeO_x nanoclusters (top) and pure CeO_2 powders (bottom). (e) Pt L_{III}-edge XANES spectrum of 0.4 wt% $Pt/CeO_x/SiO_2$ catalyst. Reproduced with permission.[67] Copyright 2022, Springer Nature. (f) The principle of controlling the size of Au NPs by lateral polarization electrochemical potential method. (g and h) SEM images of the Au/PCO samples that were annealed under various potentials: (g) −1.8 V and (h) +0.6 V for 10 min. (i) SEM images of the thermal stability for the Au NPs on the PCO support. Reproduced with permission.[68] Copyright 2022, American Chemical Society.

To further enhance the anchoring effect and charge transport ability of TMOs carrier, Liu *et al.* Prepared efficient $Pt/CeO_x/SiO_2$ catalysts by pre-confining the atomic Pt metal atoms on oxide nanoclusters or 'nanoglues' (Fig. 3a). Initially, defective CeO_x nanoglue islands were grafted onto SiO_2 with a large surface area, and the atomic Pt sites were anchored on CeO_x by the MSI effect (Fig. 3c–e). Even under harsh conditions (high temperatures, oxidizing and reducing environments), Pt atoms could remain dispersed (Fig. 3b), and the $Pt/CeO_x/SiO_2$ catalyst still exhibits markedly increased activity. The support structure and the higher affinity of Pt atoms for CeO_x than for SiO_2 were blamed for the enhanced stability under reducing circumstances, which ensures that the Pt atoms remain mobile yet stay confined to their respective nanoglue islands (Fig. 4j). This report advances metal oxide-supported single-atom catalysts one step closer to being utilized in actual applications.[67]

The adjustment of loading and size for M* in the TMOs–M* composites are of importance for the PEMFCs performance. For example, by adjusting the surface oxygen vacancy content of the TMOs support, Kim *et al.* indicated an electrochemical method to optimize the size of the Au NPs (Fig. 3f), where two kinds of supports (such as $La_{0.8}Ca_{0.2}MnO_{3\pm\delta}$ (LCM) and $Pr_{0.1}Ce_{0.9}O_{2-\delta}$ (PCO)) with different reducibility are firstly provided. By means of applying the electrochemical potential, they achieve a wide variety of effective oxygen pressures in these two supports. After the application of the cathodic potential, a high concentration of oxygen vacancies could be formed in supports, which prompt the distribution of Au NPs (7–13 nm) (Fig. 3g), while the anodic potential could oxidize the TMOs surface and increase the size of the Au NPs (Fig. 3h). The onset cathodic potential required in the creation of small Au NPs depends strongly on the reducibility of the support oxide. Finally, the Au NPs in the resulting Au NPs@LCM and Au NPs@PCO catalysts did not undergo sintering under the conditions (700–770 °C and cathodic potential) and were also stable after the catalytica process (Fig. 3i).[68]

3.1.3 Modified transition metal oxide carriers. To compensate for the shortcomings of the pristine TMOs carriers, the doping strategies and heterostructure formation are regarded as efficient methods for high-performance PEMFCs.

As for the doping strategies, metal ions with different valence states[71–73] or non-metal atoms (*e.g.*, N, S, P, B, and F)[74–76] can be doped into TMOs to optimize the electronic structure of the support. Kumari *et al.* utilized first-principles simulations to investigate microscopic Pt_n clusters ($n = 1, 2, 3$) on indium oxide (In_2O_3), Sn-doped indium oxide (ITO (111)), and hydroxylated tin-doped indium oxide ($4H_2O$-ITO(111)). It was observed that the surface energy of ITO decreased with the increase in the Sn

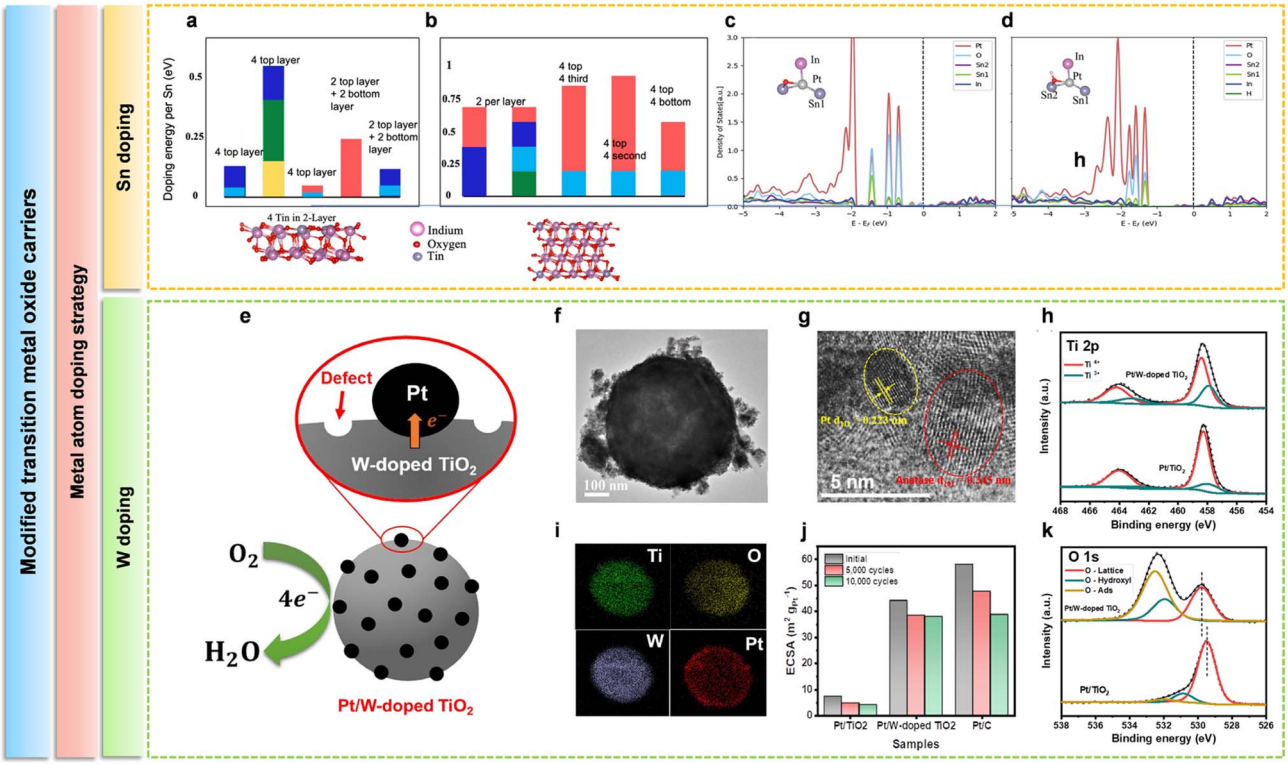

Fig. 4 (a and b) Doping energies at various sites for 5% doping in (a) 2-layer ITO and (b) 4-layer depicted by various hues. (c and d) Atom-resolved density of states projected on the atoms interacting with the Pt single atom for ITO(111) + $4H_2O$ prior to Pt deposition (c) and Pt-SA/ITO(111) + $4H_2O$ following Pt deposition (d). Reproduced with permission.[70] Copyright 2021, The Royal Society of Chemistry. (e) Scheme of Pt on W-doped TiO_2 catalyst. (f and g) HR-TEM images of Pt/W-doped TiO_2. (h) XPS comparison of Ti 2p for Pt/W-doped TiO_2 and Pt/TiO_2. (i) Mapping images of Pt/W-doped TiO_2. (j) The electrochemically active surface area (ECSA) of catalysts after ADT performed from 0.6 to 1.0 V (*vs.* RHE). (k) XPS comparison of O 1s for Pt/W-doped TiO_2 and Pt/TiO_2. Reproduced with permission.[71] Copyright 2022, Elsevier B.V.

atom doping level, which is attributed to partial Sn replacement of In surface in this bulk configuration (Fig. 4a and b). Moreover, all the Sn atoms preferred to reside at the surface layer in the instance of 5% doping; researches revealed that the presence of Sn stabilized the Pt_n cluster, especially in the case of Pt/$4H_2O$-ITO (111), which are anchored *via* the hydroxyl group. On this carrier, Pt-single atom (SA) was stabilized by ~0.5 eV on account of the Pt–cluster interaction with hydroxyls and water; however, the dimer and the trimer were not significantly stabilized. As a result, a significant amount of energy is required to form the trimer on the hydrated ITO (111) surfaces. Therefore, the sintering becomes more difficult and Pt-SA can remain metastable at moderate temperature (Fig. 4g and h). These outcomes offered a promising strategy for the development of single atom catalysts on electrically conductive substrates for electrocatalytic applications.[77]

Jinsoo *et al.* demonstrated titanium dioxide support modified by tungsten (Fig. 4e–g and i) for anchoring Pt site (Pt/W-doped TiO_2) toward ORR. In comparison to the undoped TiO_2 support, W-doped TiO_2 displayed a higher surface area, more Ti^{3+} defect sites (Fig. 4h), and oxygen vacancies (Fig. 4k), which improved the SMSI for the deposited Pt catalyst. Furthermore, a high electrochemical surface area of 44.1 $m^2\ g_{Pt}^{-1}$ and an MA value of 41.22 mA mg_{Pt}^{-1} in 0.1 M $HClO_4$ further revealed the high ORR activity of the Pt/W-doped TiO_2 catalyst. Additionally, the rotating ring-disk electrode (RRDE) measurements of the Pt/W-doped TiO_2 catalyst under acidic circumstances revealed a four-electron pathway, achieving an ultrasmall H_2O_2 yield of 0.42%. In particular, the durability test demonstrated that the Pt/W-doped TiO_2 had a exceptional remarkable stability compared with commercial catalysts (Fig. 4j).[71]

He *et al.* distributed nearly homogeneous Pt clusters using atomic layer deposition (ALD) on stable Sb-doped tin dioxide (ATO) support with highly conductive (6.2 S cm^{-1}) (Fig. 5a–c). The combination of high oxidation stability and SMSI enabled ALD-Pt/ATO to exceed the Pt/C activity and stability. Sb(v) was incorporated into the SnO_2 lattice to produce an n-type electron-rich oxide by doping Sb. Since Sn (1.8) is less electronegative than Pt (2.2), more electrons prefer to stay in the Sn position in the Pt–O–Sn system than in the Sn–O–Sn system, causing the Sn K edge to migrate toward the lower energy side (Fig. 5d). This indicates that Pt interacts with Sn sites, changing the electronic state of Sn and increasing the availability of electrons at the Pt sites. After Pt on ATO underwent ALD, the Pt L3 edge peak intensity decreased and fell below the Pt/C, demonstrating an extensive electron transfer from support to Pt (Fig. 5e) and thus confirming the presence of SMSI. Meanwhile, the SMSI between the Pt cluster and ATO-enabled ALD-Pt/ATO showed a significantly higher ECSA (74 $m^2\ g^{-1}$) and MA (102 mA mg_{Pt}^{-1} at 0.9 V *vs.* RHE) for the ORR process. Hence, it was discovered that the

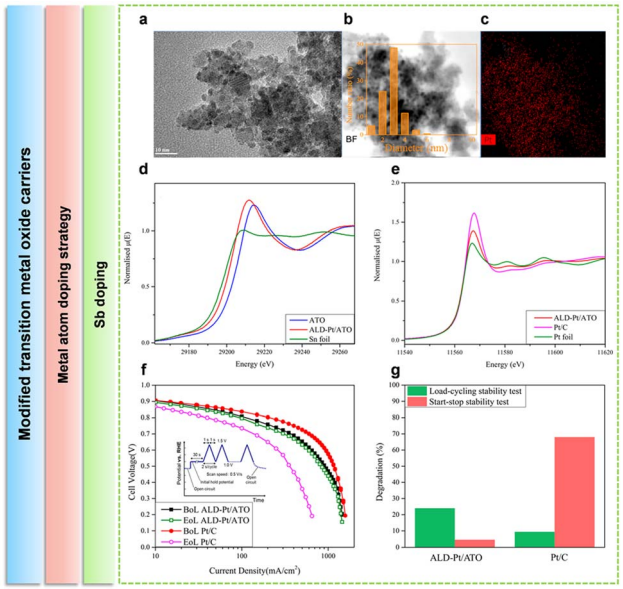

Fig. 5 (a–c) Effect of the deposition technique on the size and dispersion of Pt particles. Image of TEM (a), STEM (b), and EDX mapping (c). (d and e) Electronic interactions of the catalyst-support. Sn K edge with Sn metal foil (d) and Pt L3 edge along with Pt metal foil and PtO_2 (e) normalized XANES spectra. (f) Performance of MEAs prepared utilizing Pt/C at the anode and Pt/C and ALD-Pt/ATO at the cathode for H_2-air fuel cell before and after AST using start-stop protocol. (g) Percentage of the peak power density losses after 1000 start-stop stability tests and 5000 loading cycling stability tests. Reproduced with permission.[70] Copyright 2022, American Chemical Society.

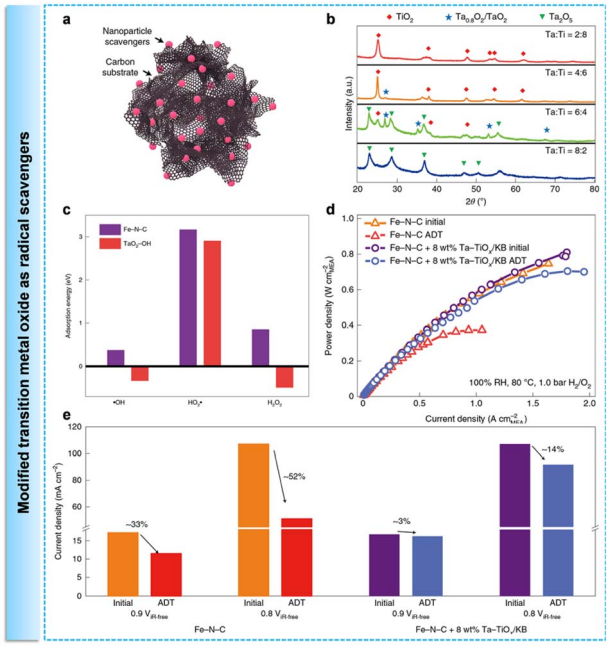

Fig. 6 (a) Diagram demonstrating the well-distributed Ta–TiO_x nanoparticles on the carbon support as scavengers. (b) XRD images of the nanoparticles manufactured with Ta to Ti ratios of 2 : 8, 4 : 6, 6 : 4, and 8 : 2. A rutile tantalum oxide phase was discovered when the ratio was 6 : 4. (c) Adsorption energies of H_2O_2 and related radicals on the surfaces of Fe–N–C and TaO_2–OH. (d) Current density decay comparison for cells with and without Ta–TiO_x/KB after the ADT. (e) Power density polarization for cells prior to and after the ADT. Reproduced with permission.[73] Copyright 2022, Springer Nature.

change in the ALD-Pt/ATO performance was negligible after 1000 start-stop potential cycles (Fig. 5f), demonstrating excellent stability (Fig. 5g).[70] Besides, recent study suggested that metal atom doped transition metal oxides have other new applications in PEMFCs. For instance, Xie *et al.* demonstrated that Ta–TiO_x nanoparticle additives protect Fe–N–C catalysts from such degradation *via* radical scavenging. First of all, the 5 nm Ta–TiO_x nanoparticles were uniformly synthesized on a Ketjenblack substrate (Fig. 6a), and forming the rutile TaO_2 phase (Fig. 6b). In particular, TaO_2 is more competitive at capturing H_2O_2 and related radicals due to TaO_2–OH(110) surface has stronger adsorption energies than Fe–N–C for H_2O_2 and related radicals ($\cdot OH$ and $HO_2\cdot$) (Fig. 6c), which can help impede their attack to the Fe–N–C active sites. It is found that a fuel cell prepared with the scavengers showed a current density decay of 3% at 0.9 V (a fuel cell without scavengers showed 33% decay) (Fig. 6d), exhibiting improved durability (Fig. 6e).[73]

As for the heterostructures strategies, the incorporation of other conductive supports[78,79] could improve the electrical conductivity, optimize the adsorption/desorption of ORR intermediates, and ultimately enhance the overall electrochemical properties on the heterojunction interfaces. In addition, the formation of heterostructures could also introduce defects sites, which are conducive to anchor the active metal atoms.[80] Lin *et al.* reported a novel SnS_2/SnO_2 heterostructure-supported Pt NPs for ORR, where Pt NPs are primarily deposited at the interfaces of SnS_2 and SnO_2 moiety contacts (Fig. 7a). The concentration of the heterointerfaces can tune the SMSI between Pt and SnS_2/SnO_2 (Fig. 7b), which can speed up the electronic transfer and enrich the electron density of Pt with a beneficial shift of the d-band center (Fig. 7c and d). In electrochemical ORR measurements, the MA of the optimal Pt–SnS_2/SnO_2 catalyst is four times higher than that of Pt/C at 0.9 V *versus* RHE (400 mA mg_{Pt}^{-1}). Also, Pt–SnS_2/SnO_2-90 displays the highest ORR activity ($E_{1/2}$ = 0.895 V) (Fig. 7e). Regarding stability, after 5000 potential cycles at a high potential region (1.0–1.6 V), the MA and ECSA of Pt–SnS_2/SnO_2 barely dropped by 18.2% and 23.7%, respectively (Fig. 7f and g).[79] Chen *et al.* synthesized a $SrMn_3O_{6-x}$–$SrMnO_3$ (SMO_x–SMO) heterostructure through epitaxial growth techniques. The adsorption and desorption of ORR intermediates on the heterojunction surface are optimized by the creation of high-valence $Mn^{3+/4+}$, assisting in encouraging a favorable change in the location of the d-band center, which showed outstanding ORR electrocatalyst performance.[81]

3.2 Transition metal carbide carriers (TMCs)

Recently, TMCs have arisen as attractive materials in the realm of heterogeneous catalysis due to their abundant reserves, accessible price, and unique physical/chemical properties. For example, the DFT result has shown that the introduction of carbon in TMCs can change the lattice constant of the early

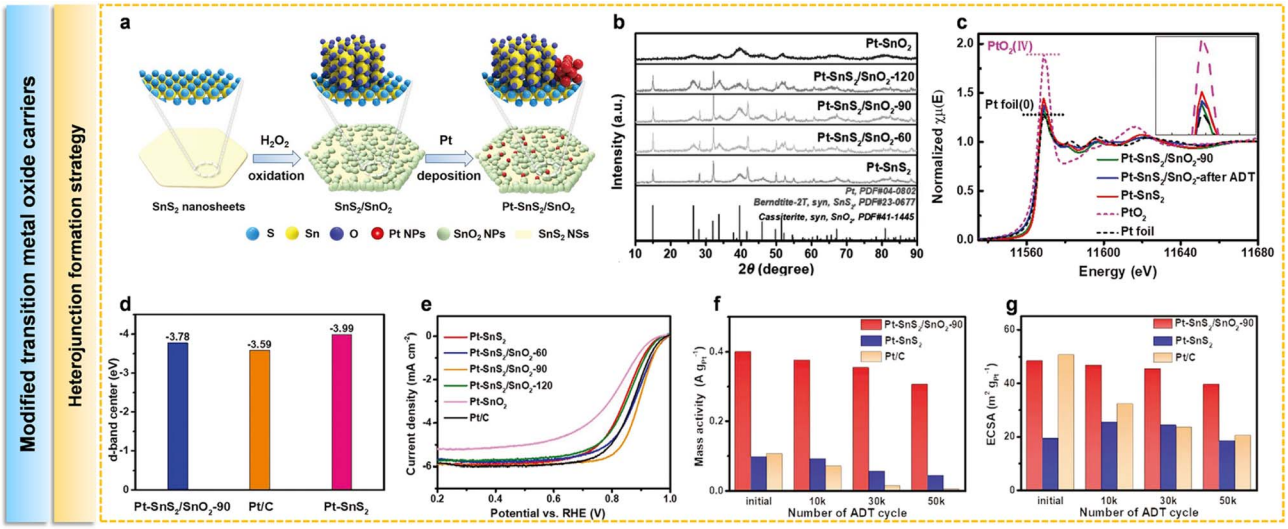

Fig. 7 (a) Schematic illustrating the synthesis pathway to Pt–SnS_2/SnO_2. (b) HR-TEM images of Pt–SnS_2/SnO_2-90. (c) Pt L3-edge XANES spectra. (d) The d-band center for Pt–SnS_2/SnO_2-90, Pt/C, and Pt–SnS_2, respectively. (e) Polarization curves of Pt/C, Pt–SnS_2, Pt–SnO_2, and Pt–SnS_2/SnO_2 samples in O_2-saturated 0.1 M $HClO_4$ at 1600 rpm and 10 mV s^{-1} for ORR. (f) MA and (g) ECSA values of Pt–SnS_2/SnO_2-90, Pt/C, and Pt–SnS_2 before and after ADT. Reproduced with permission.[79] Copyright 2022, Wiley-VCH GmbH.

transition metals, which have a significant impact on their physical/chemical properties, such as electronic interaction between the parent TM and valence states of C, metal–metal distance, d-band of TM.[82,83] All these effects endow the TMCs with unique electrochemical activity compared to the parent TM. Yet, this enhancement in activity is not high enough to catalyze the practical electrochemical process, for example, PEMFCs and electrochemical water splitting. Alternatively, TMCs materials are always seen as the potential supports for the dispersion of highly active metal sites (*e.g.*, platinum group

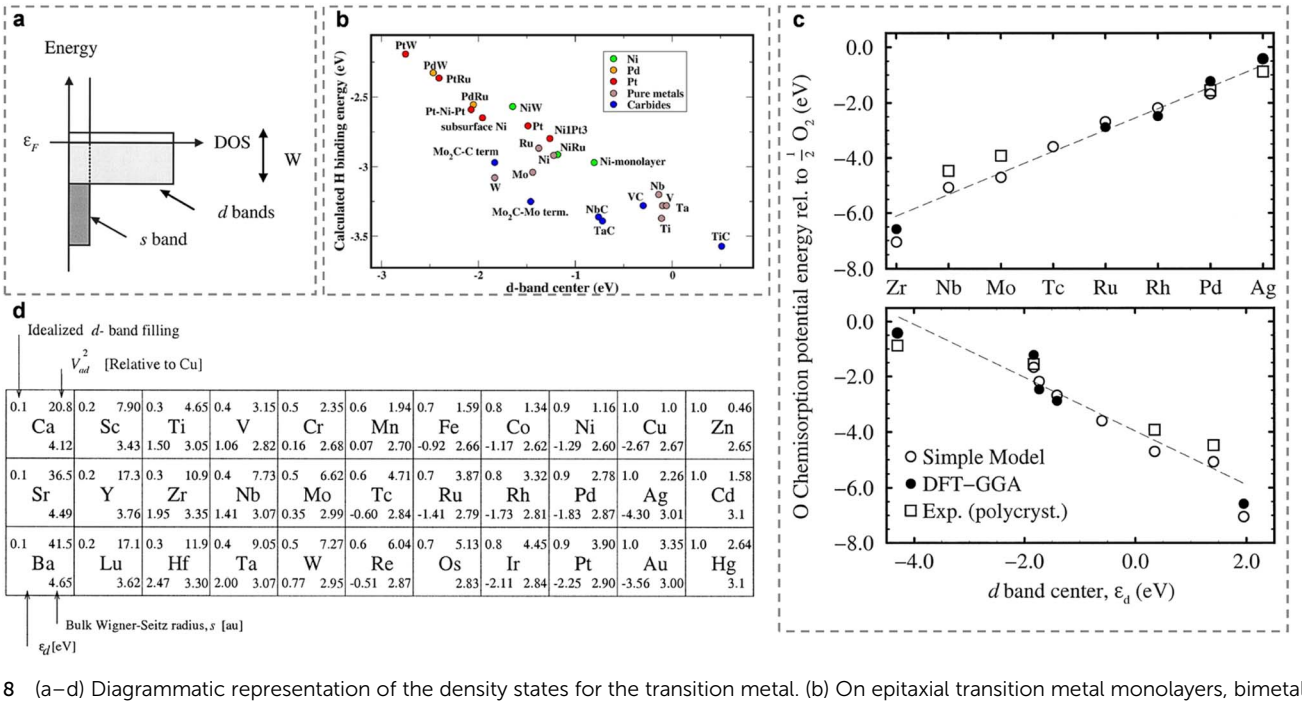

Fig. 8 (a–d) Diagrammatic representation of the density states for the transition metal. (b) On epitaxial transition metal monolayers, bimetallic sandwich structures, surface alloys, early transition metal, and carbide surfaces; the short d-band center and hydrogen binding energy are correlated. (c) Comparison of oxygen chemisorption energies based on DFT. The good correlation between calculated adsorption energies and the d-band center ε_d (bottom). (d) Section of the periodic table with the 3d, 4d, and 5d transition metals. In the upper left corner, the idealized d-band fillings are shown. The transition metals 3d, 4d, and 5d are located in this section of the periodic chart. The d-band fillings are illustrated in their idealized form in the upper left corner. Reproduced with permission.[87] Copyright 2000, Academic Press.

metals). Based on the similarity of the electronic structure between platinum group metals and TMCs, the obtained TMCs-based composites could possess attractive activity for different electrochemical systems. Especially in the PEMFCs application, due to their unique electrochemical activity, excellent mechanical/chemical durability, high electrical conductivity, and tunable MSI effect TMCs have become one of the most potential alternative carbon-free supports for PEMFCs.[84–86]

3.2.1 MSI effect between TMCs and M*. B. Hammer has demonstrated that the center, the filling, and the width of the d-band play a key role in the adsorption and activation of the reactants. In general, the d-band width of non-precious metals is narrower than that of precious metal Pt, while their d-band filling degree is less than that of Pt (Fig. 8a and d).[87] Meanwhile, the metal density of states (DOS) near the Fermi level can be modified by the electronic interaction between the valence states of carbon and the parent metal (Fig. 8b). Particularly in the TMCs, the hybridization of d-orbitals (transition metal) with s/p orbitals (carbon) can broaden the d-band structure of transition metals,[88–90] which results in TMCs having suitable oxygen chemisorption energies and better ORR activity than pure metals (Fig. 8c). Furthermore, TMCs have a similar electronic structure to Pt group metals near the Fermi level, which have became one of the most attractive supports for ORR,[88,91] which promoted electron transfer between metal and the carbide TMCs supports, optimizing their stability and intrinsic activity for PEMFCs.[99]

3.2.2 Pristine transition metal carbide carriers. Levy and Boudart firstly discovered the similarity between TMCs and Pt group noble metals,[83] and the interface (Pt–TMC)-induced electron transfer could enhance the intrinsic ORR activity of Pt–TMC.[88] Based on this, TMCs were initially regarded as the electron activator for improving the electrocatalytic activity of the classic Pt/C by constructing a series of Pt–TMCs/C catalysts such as Pt-WC/C[92] and Pt–MoC/C.[93] Although their ORR activity could be enhanced due to the synergistic effects of various components, the issues of poor stability are still not solved well.[94,95] Since then, several efforts have been made to engineer TMCs-based support catalysts with the aim of modulating their microstructure, shape, composition, and sur/interfaces to enhance the MSI, thereby increasing their activity and durability.[96,97]

Bott-Neto *et al.* synthesized cubic phase β-WC_{1-x} ($0.34 < x < 0.43$) nanomaterials with an average size of 1.65 nm, which were utilized for the synthesis of the Pt-tungsten carbide-based catalysts (Pt-β-WC/C_{1-x}). Pt NPs were homogeneously distributed on the β-WC_{1-x}. The Pt-XANES results revealed a slight rise in the Pt 5d band occupancy, which may lead to a weaker Pt-OH_x interaction and increased the ORR kinetics in the acidic medium.[92] Hamo *et al.* electrodeposited $PtCl_6^{2-}$ onto an α-Mo_2C support at different overpotentials (η). When Pt is deposited in the lower overpotentials (+8 and +18 mV *vs.* SCE), a large number of uniform-dispersed Pt crystals (less than 2 nm) can be found on the Mo_2C support. Hence, excellent ECSA and MA (for

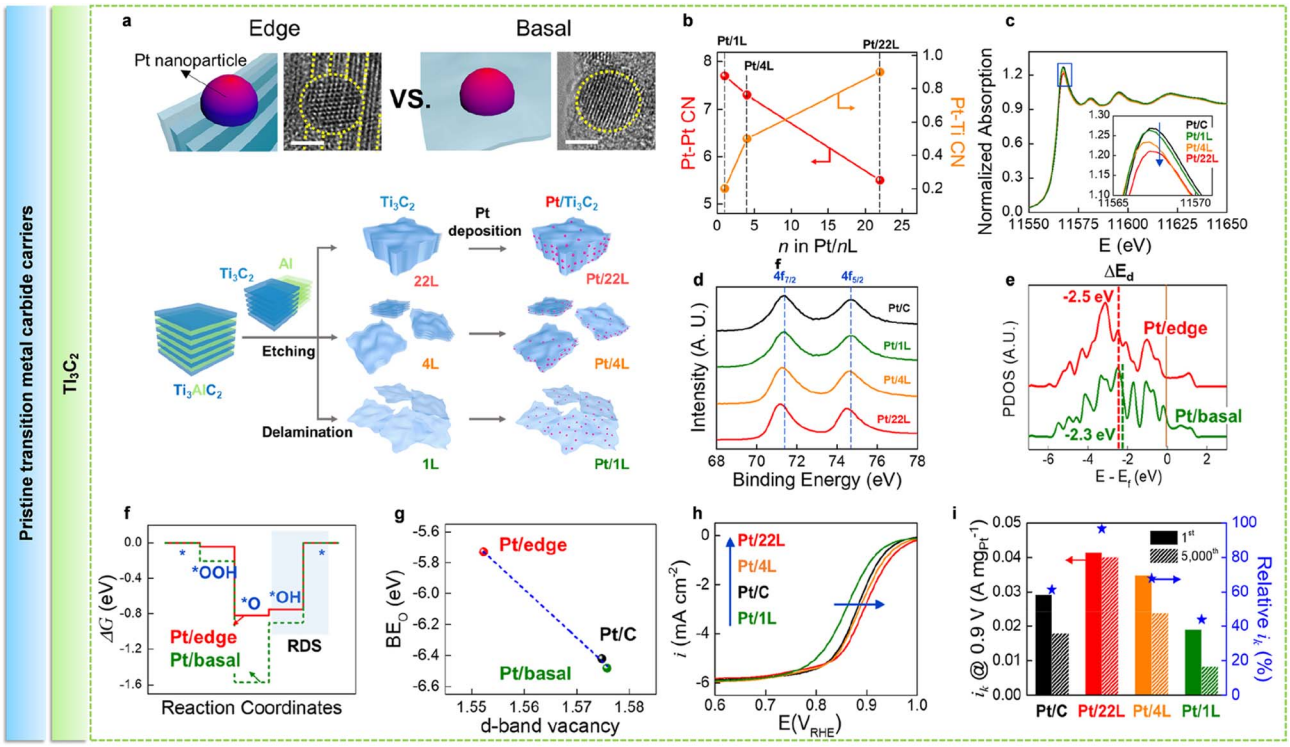

Fig. 9 (a) Platinum nanoparticles loaded on two-dimensional Ti_3C_2 (Pt/Ti_3C_2). (b) Coordination numbers (CNs) of Pt–Ti and Pt–Pt. (c) XANES spectra of Pt L3-edge. (d) XPS spectra of Pt 4f. (e) Average projected density of states (PDOS) of d states for Pt_{13}. E_f = energy at the Fermi level; ΔE_d = d-band center. (f) Free energy diagram of ORR at $U = 1.23$ V. (g) Binding energy of oxygen (BE_O) in relation to the d-band vacancy measured by XANES. (h) ORR polarization curves in the oxygen-saturated acid media of 0.1 M $HClO_4$. (i) ADT to measure the ORR current retention along cycles. Reproduced with permission.[108] Copyright 2020, Elsevier Ltd.

ORR) were observed in this catalyst, which are superior to the catalysts prepared in a higher overpotentials (−67 and −92 mV *vs.* SCE). In fact, catalysts synthesized in the low-overpotential region could achieve an MA of 275 mA mg_{Pt}^{-1} for ORR, which have broken the reported linear relationship between MA and Pt loading. To further explore the stability of the obstacle catalyst, they also prepared contrast catalysts by the chemical reduction of Pt onto α-Mo_2C and Vulcan XC-72. Also, they found that the catalyst prepared in the low-overpotential region exhibited the best stability after the accelerated stress test (AST, 5000 cycles) among all the contrast samples.[98] In addition, Lee et al. selected highly conductive two-dimensional titanium carbide (Ti_3C_2) as the support for Pt because of the expected SMSI between Pt and Ti_3C_2. Pt nanoparticles (4 nm) were loaded on three different Ti_3C_2 supports including multi-, few-, and mono-layered Ti_3C_2 (Fig. 9a). The edge-to-basal ratio of layered Ti_3C_2 changed obviously with the increase of layers number (Fig. 9b). As shown in Fig. 9c–e, the edge-dominant support (22L-Ti_3C_2) donated more electrons to Pt than the basal-dominant supports (4L-Ti_3C_2 and 1L-Ti_3C_2). The thermodynamic barrier of Pt/edge was lower than that of Pt/basal, which can be originated from the difference in the electronic configuration of Pt tuned by the support planes (Fig. 9f). In addition, Fig. 9g further verified the weaker binding of oxygen species to the Pt surface for Pt/edge, compare to the Pt/basal catalyst. In summary, the increase in the free energy of *O and the enhancement of OH desorption in Pt leaded to the highest ORR electroactivity of Pt/edge (Fig. 9h). In addition, the electron transfer from the support to Pt inducing the strong MSI between Pt and Ti, further improving the durability of the ORR electroactivity of Pt (Fig. 9i).[108]

3.2.3 Modified transition metal carbide carriers. Though transition metal carbide carriers have numerous advantages, they suffer from the drawback of thermodynamic instability under oxidative fuel cell conditions. Particularly under the voltage spikes caused by startup/shutdown, the stability windows would be limited for a majority of TMCs, such as Mo_2C and W_xC. In this case, transition metal carbides are at risk of being transformed into transition metal oxides, which are more thermodynamically stable.[100,101] Therefore, in order to take full advantages of TMCs in the catalytic ORR process, it is necessary to design and synthesize the modified TMCs catalysts by constructing TMCs-based composites, heteroatom-doped TMCs, optimizing the microstructure of TMCs, *etc.*[82,102]

He *et al.* assembled Pt nanoparticles on a two-dimensional Co_6Mo_6C nanosheets/reduced graphene oxide hybrid (Pt/Co_6Mo_6CNSs-G) as the PEMFC cathode catalyst. As exhibited in Fig. 10a, the Pt nanoparticles are anchored on the Co_6Mo_6CNSs-G support tightly to generate abundant and stable Pt/Co_6Mo_6C heterojunction interfaces that can be found in Pt/Co_6Mo_6CNSs-G. Furthermore, due to the uniform dispersion of Pt nanoparticles, several Pt–TMC-RGO interfaces were also constructed at the same time. XANES technologies confirmed that the electron coupling synergy between Pt and TMC can be highly optimized (Fig. 10b). Finally, the ORR activity and stability of Pt/Co_6Mo_6CNSs-G can be improved compared to the contrast samples, which outperformed the commercial Pt/C (Fig. 10c and d). All these results demonstrated the importance of the Pt/Co_6Mo_6CNSs-G heterojunction-induced electron coupling effect for efficient ORR performance.[103]

Hamo *et al.* synthesized an $Mo_{85}Ta_{15}$ alloy (Fig. 10e and f) by the method of co-reduction carburization, which has optimized activity and corrosion resistant. Briefly, the addition of 15 mol% Ta to the precursor mixture can increase the corrosion potential by ∼150 mV and decrease the corrosion current to 16%.[106]

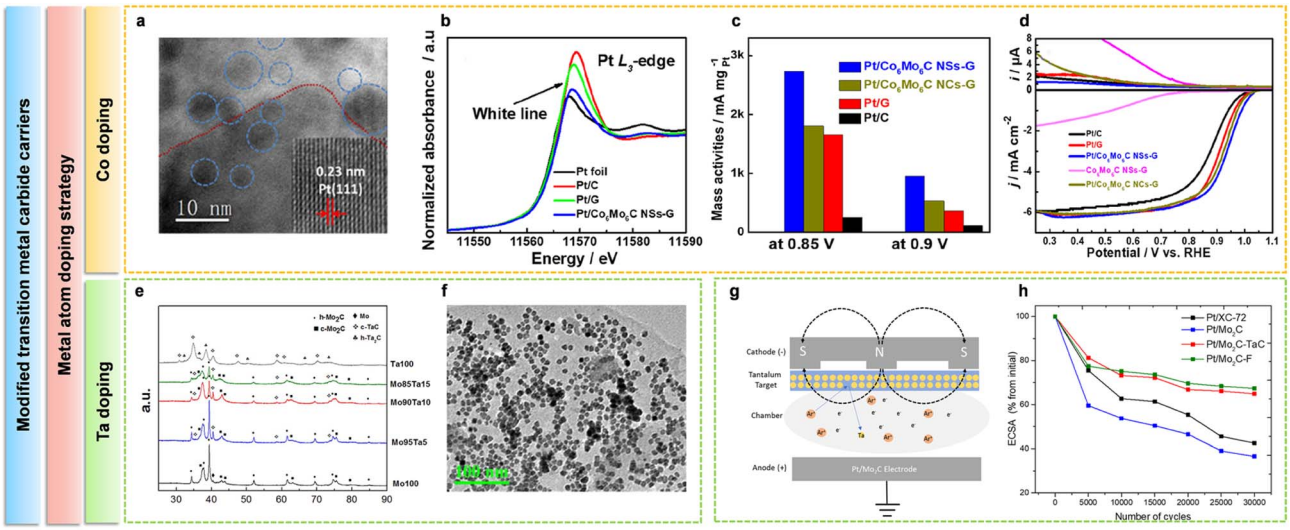

Fig. 10 (a) HRTEM images of Pt/Co_6Mo_6C NSs-G, (b) XPS results of the Pt 4f of Pt/C, Pt/G, and Pt/Co_6Mo_6C NSs-G, (c) comparison of MA of Pt/C, Pt/G, Pt/Co_6Mo_6C NSs-G, and Pt/Co_6Mo_6C NCs-G at 0.85 V and 0.9 V. (d) Evaluation of the ECSA decline for Pt/C, Pt/G, and Pt/Co_6Mo_6C NSs-G during the ADT. Reproduced with permission.[103] Copyright 2022, American Chemical Society. (e) XRD patterns of carbide supports, along with molybdenum precursor mixtures with 5, 10, and 15 wt% tantalum. (f) TEM of Pt_3Ni octahedral dispersed on a $Mo_{85}Ta_{15}$ support. Reproduced with permission.[106] Copyright 2019, The Electrochemical Society. (g) Composite diagram of Pt/Mo_2C–F. (h) ECSA loss during AST. Reproduced with permission.[107] Copyright 2021, Wiley-VCH.

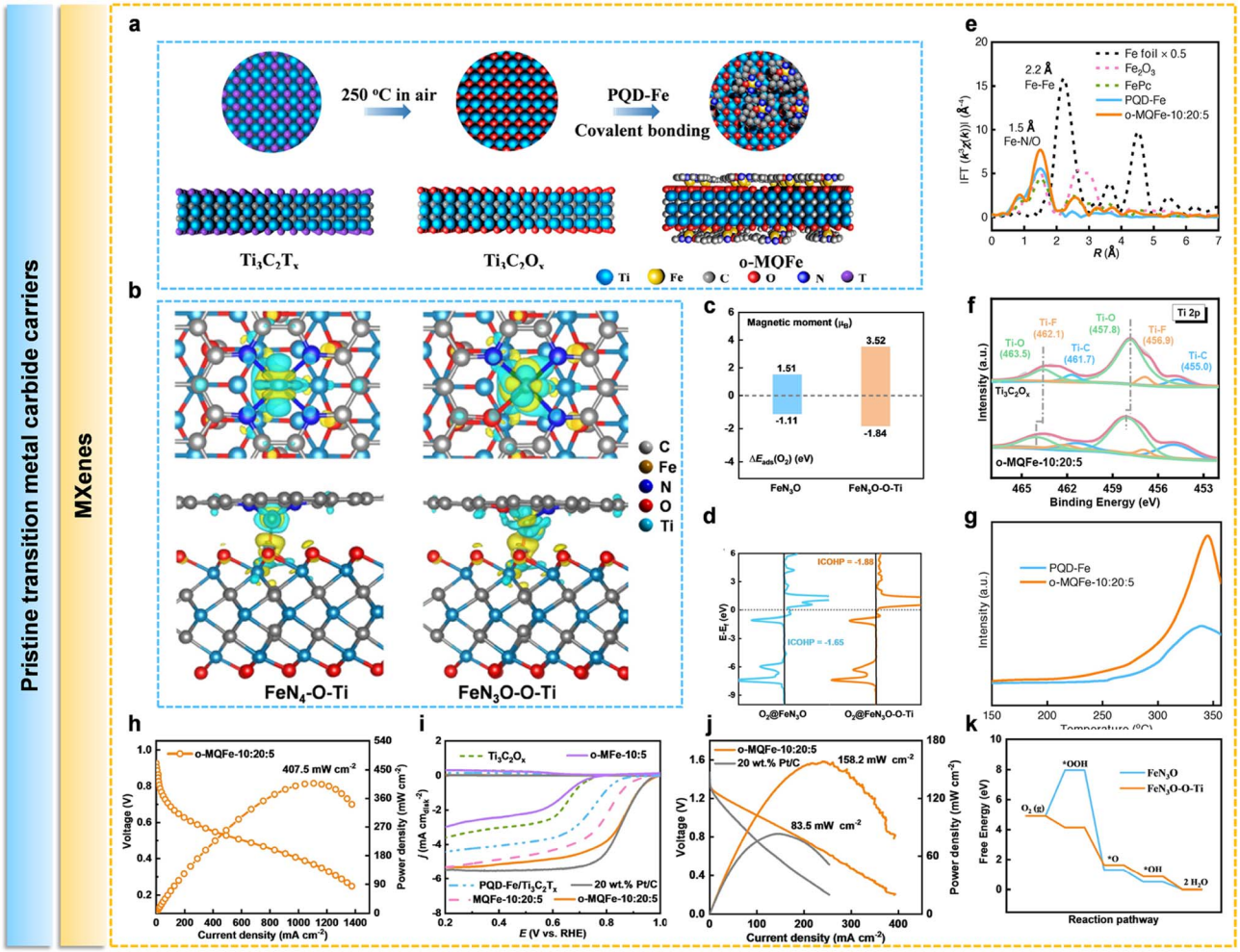

Fig. 11 (a) The synthesis process of o-MQFe. (b) Charge density distributions of FeN_3O–O–Ti and FeN_4–O–Ti within and (c) the μ_B and $\Delta E_{ads}(O_2)$ values and (d) ICOHP value of FeN_3O and FeN_3O–O–Ti. (e) Fe K-edge XANES, (f) XPS Ti 2p spectra, and (g) O_2-TPD curves, and (h) LSV curves for different catalysts. Polarization and power density curves of (i) ZABs and (j) H_2/O_2 AEMFCs performance. (k) The calculated free energy changes. Reproduced with permission.[115] Copyright 2022, Wiley-VCH GmbH.

Furthermore, DFT calculations confirmed the higher the corrosion resistance of $Mo_{85}Ta_{15}$ by comparing the oxygen binding energies of all the contrast models, which further demonstrated that the durability of transition metal carbide carriers can be improved by adding metals with high oxygen binding energy (*e.g.*, Ta).[104,105] After that, Pt_3Ni have been synthesized on the surface of the $Mo_{85}Ta_{15}$. The octahedral Pt_3Ni nanoparticles are highly dispersed on the $Mo_{85}Ta_{15}$ support, which exhibit excellent $E_{1/2}$ at 1200 rpm and MA (240 mA mg_{Pt}^{-1}) for ORR. It is suggested that such materials may act as a viable replacement for carbon supports in PEMFCs.[106] In the later study, Hamo *et al.* further modified Mo_2C support by surface Ta treatment *via* DC magnetron sputtering techniques (Fig. 10g). Compared with untreated supports, all the supports modified by Ta displayed enhanced corrosion resistance. Meanwhile, the best Ta-modified Pt/Mo_2C composites (Pt/Mo_2C–F) showed improved dynamic current density and MA for ORR. XPS indicated that none of the Ta carbide phase formed in this sputtered samples. Meanwhile, trace Ta_2O_5 can be found on the surface of Pt/Mo_2C–F, which played a role in restricting the loss of electrochemical surface area and the formation of voids. Finally, Ta-doped Pt/Mo_2C membrane was further used to assemble the PEMFCs device, showing a significantly improved durability after the AST test (Fig. 10h). Such a result demonstrates that without sacrificing the ORR kinetics, Ta alteration by magnetron sputtering can increase the oxidation potential, which is different from other reported TaC-modified Mo_2C composites (TaC–Mo_2C).[107]

Besides, the 2D transition-metal carbides, especially MXenes (such as Ti_2CT, where T represents functionalized termination),[109,110] have been considered as a potential support for the cathode catalyst of the fuel cell because of their metallic conductivity, electrochemical stability, and surface-charge property.[111–114]

Our group prepared a MXene-based catalyst (o-MQFe) with FeN_3O–O–Ti configurations, obtained from polymer-like quantum dots with atomic Fe (PQD-Fe) anchored on the O-terminated MXene ($Ti_3C_2O_x$) surface as a cathode for AEMFCs

(Fig. 11a). Density functional theory (DFT) calculations demonstrate that the existence of axial Fe–O–Ti ligands can translate the low-to-medium spin state of Fe catalytic centers and optimize O_2 adsorption, thus improving the ORR performance (Fig. 11b). As shown in Fig. 11c, the values of magnetic moment (μ_B) and O_2 adsorption energy ($\Delta E_{ads}(O_2)$) are 1.51 μ_B and −1.11 eV for FeN_3O (without axial Fe–O–Ti ligands) and 3.52 μ_B and −1.84 eV for FeN_3O–O–Ti, respectively, illustrating the preferable e_g filling and O_2 adsorption. This moderate O_2 binding strength can also be reflected by integrated-crystal orbital Hamilton population (ICOHP) results (Fig. 11d). The binding strength can also be reflected by integrated-crystal orbital Hamilton population (ICOHP) results (Fig. 11d). As a proof-of-concept, the axial Fe–O–Ti ligands are constructed in the o-MQFe catalyst, confirmed by fitting the extended X-ray adsorption fine structure (EXAFS) and XPS spectra. The local

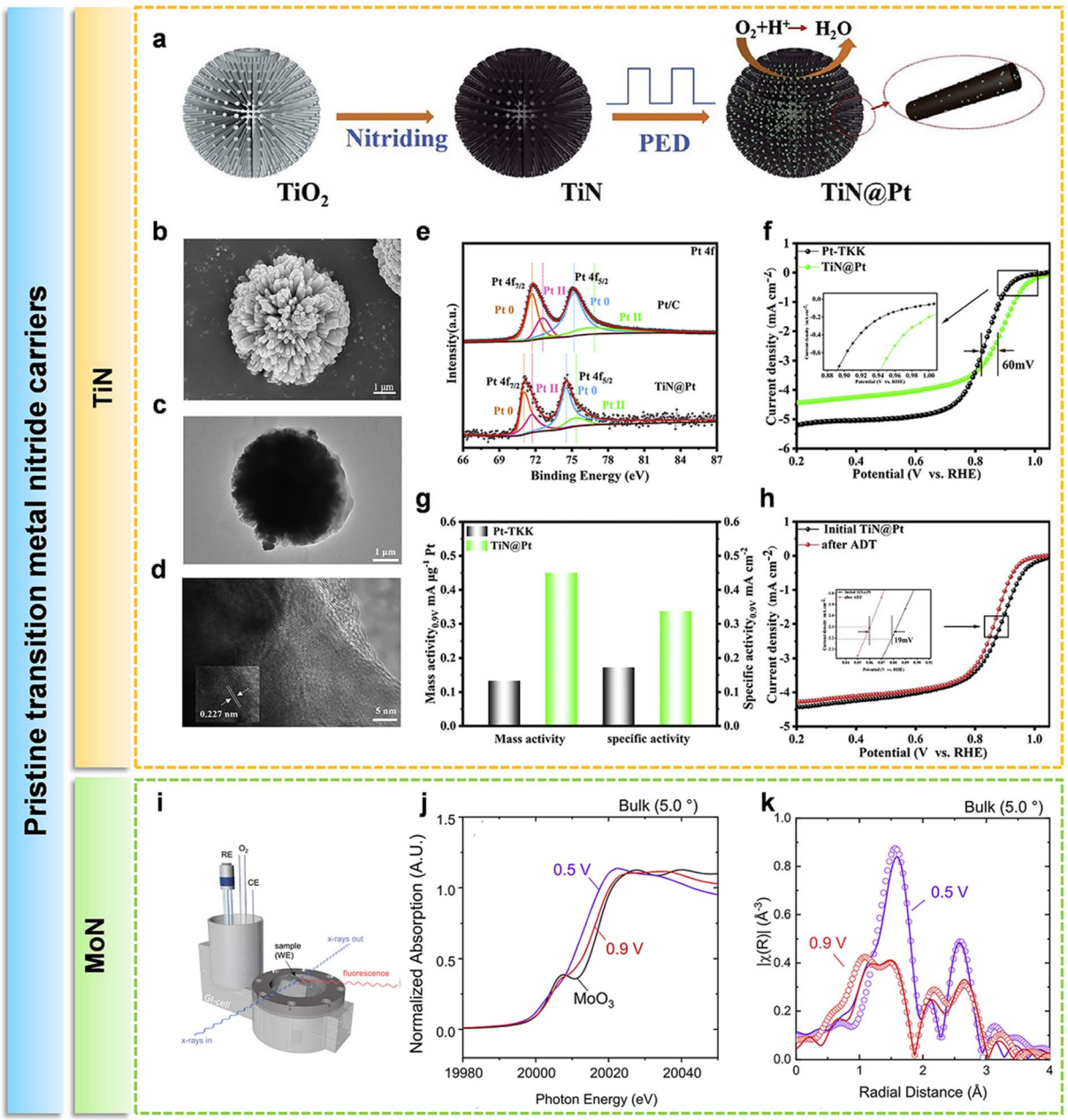

Fig. 12 (a) Synthesis route on of TiN@Pt Ns. (b) SEM images of TiNNs. (c) TEM image of a single TiN@Pt Ns, (d) TEM image of Pt, inset: HRTEM image of corresponding. (e) XPS spectra of various samples at point 4f. (f) ORR polarization curves of catalysts recorded with rotating disk electrode (RDE) at 1600 rpm and a scan rate of 10 mV s^{-1} in 0.1 M $HClO_4$ solution saturated with O_2. (g) Mass and specific activities for TiN@Pt and Pt/C. (h) Polarization curves for TiN@Pt before and after the ADT test. Reproduced with permission.[127] Copyright 2022, Hydrogen Energy Publications LLC. (i) Schematics of the *in situ* GI-cell. Bulk (5.0°). (j) XANES and (k) EXAFS for Mo K-edge at 0.5 V and 0.9 V *vs.* RHE. Reproduced with permission.[128] Copyright © 2020 American Chemical Society.

chemical environment of the Fe center in o-MQFe is the Fe–N_3O asymmetric coordination (Fig. 11e), and the positive shift of the Ti–F bond in the Ti 2p XPS spectra indicates the electronic redistribution induced by axial Fe–O–Ti ligands (Fig. 11f). The O_2 adsorption affinity of the o-MQFe catalyst can be judged by the intensity of the O_2-desorption peaks of O_2 temperature-programmed desorption (O_2-TPD) curves; the higher intensity of o-MQFe-10 : 20 : 5 manifests its stronger O_2 affinity compared with the control sample without axial Fe–O–Ti ligands (Fig. 11g). The optimal o-MQFe-10 : 20 : 5 catalyst shows a good ORR activity, a $E_{1/2}$ value of 0.861 V *vs.* RHE, higher than that of Pt/C and other most reported MXene-based catalysts (Fig. 11h). Notably, the assembled AEMFC and ZAB with o-MQFe-10 : 20 : 5 as the cathode catalyst deliver high rated powers in a wide-temperature range (Fig. 11i and j). DFT calculations reveal that the formed axial Fe–O–Ti ligands in FeN_3O–O–Ti lowers the exothermic energy barrier of the potential determining step in contrast with FeN_3O, thus enhancing the ORR activity (Fig. 11k).[115]

3.3 Transition metal nitride carriers (TMNs)

Transition metal nitrides are formed by the incorporation of nitrogen atom into the interstitial transition metal network. As reported in previous researches, TMNs have unique physical and chemical characteristics, such as high melting points, hardness, and corrosion resistance. Moreover, TMNs have unique electronic and mechanical properties, which endow TMNs with extremely important applications in the field of electrocatalysis and material sciences.[116,117] Since the first successful exploration of tungsten nitride (WN)-based ORR catalyst with a high stability (in excess of 1000 cycles),[118] a mass of TMNs have been accordingly designed for PEMFC cathode catalyst carriers.

3.3.1 MSI effect between TMNs and M*. After the formation of TMNs, the d-band characteristics of the parent transition metal can be well altered, including the d-band contraction and higher DOS near the Fermi level, which is similar to the Pt-based precious metals. Based on this, TMNs are expected to be used as catalyst support for platinum and other metals in the PEMFC cathode instead of traditional carbon supports. Firstly, TMNs have high electrical conductivity, enabling high charge transfer during catalysis across a broad potential range.[119–121] Secondly, the MSI between TMNs and active metals is stronger than that between other carbon carriers and active metals. Moreover, the decrease in the d-band leads to a higher DOS within the Fermi level and faster charge transfer.[122] Meanwhile, due to the SMSI between TMNs and active metals, higher dissolution potential, higher surface strain, and lower binding energy of O and OH can be found in TMNs–M*, which accordingly prompt their ORR performance.[123–126]

3.3.2 Pristine transition metal nitride carriers. In general, TMNs are more stable than metal carbides operated under the harsh conditions of high voltage and acidic media for PEMFCs application. Therefore, it was more intriguing to be regarded as

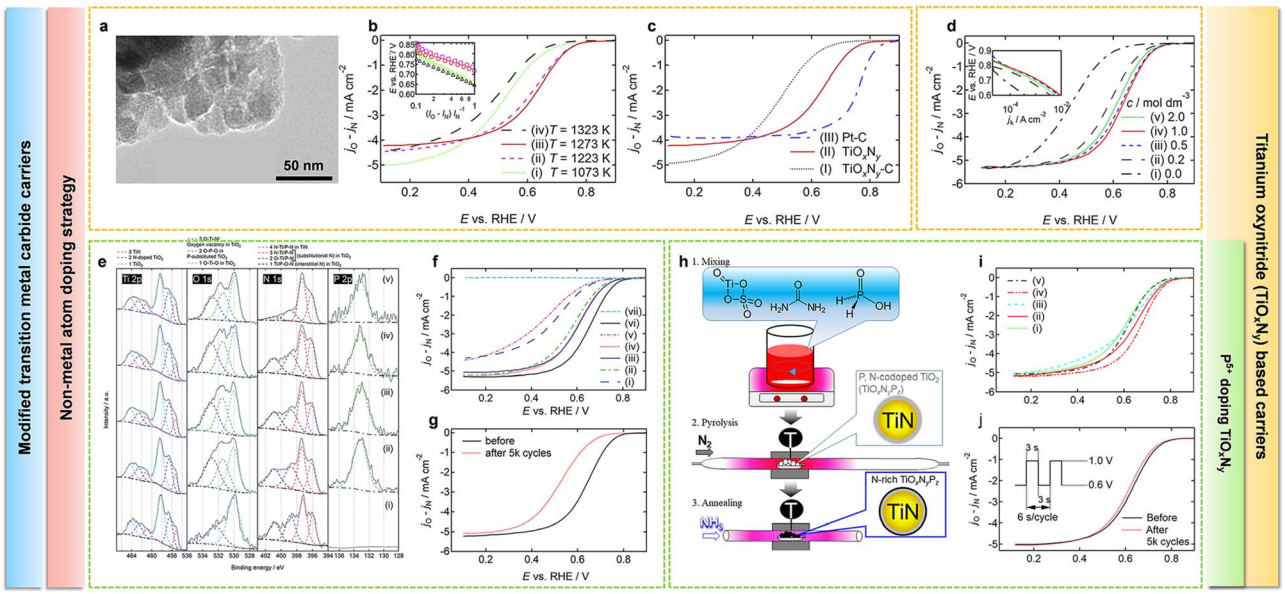

Fig. 13 (a) TEM image of TiO_xN_y. (b) RDE voltammograms of TiO_xN_y after pyrolysis at four different temperatures. The inset in (b) shows the Tafel plots using normalized current. (c) RDE voltammograms of (I) TiO_xN_y–C, (II) TiO_xN_y, and (III) Pt–C. Reproduced with permission.[129] Copyright 2016, Elsevier Ltd. (d) RDE voltammograms of TiO_xN_y catalysts for five different c values. Reproduced with permission.[130] Copyright 2017, American Chemical Society. (e) X-ray photoelectron (XP) spectra of Ti 2p, O 1s, N 1s, and P 2p for $TiO_xN_yP_z$ catalysts with five different R_P (the atomic ratio of phosphor to titanium). (f) RDE voltammograms of $TiO_xN_yP_z$ catalysts with five different R_P. (g) RDE voltammograms of $TiO_xN_yP_z$ (R_P = 0.5) catalyst before and after 5000 potential cycles between 1.0 and 1.5 V. Reproduced with permission.[131] Copyright 2019, The Royal Society of Chemistry. (h) Scheme for the three-step synthesis of $TiO_xN_yP_z$ catalysts. (i) RDE voltammograms of the $TiO_xN_yP_z$ catalysts synthesized using the new phosphorus source, H_3PO_2. (j) RDE voltammograms of the $TiO_xN_yP_z$ (R_P = 0.20) catalyst between 1.0 and 1.5 V in 0.1 mol dm^{-3} H_2SO_4 solution before and after 5000 potential cycles test. Reproduced with permission.[132] Copyright 2020, American Chemical Society.

supports for the ORR catalyst. Commonly, the optimized ORR activity for TMNs–M* can be attributed to the reduced size of the TMNs nanoparticles, the enrichment of the d orbital with electrons, and the enhanced oxygen adsorption.[84]

Yuan *et al.* synthesized a dandelion-like framework of TiN nanospheres with abundant dendritic structures as a carrier for Pt nanoparticles (TiN@Pt Ns) by an electrochemical pulse deposition method (Fig. 12a–c). The HRTEM image in Fig. 12d showed the lattice stripe spacing (0.227 nm) of the Pt (111) plane, confirming that a thin Pt layer was successfully applied on the surface of TiN. As shown in Fig. 12e, in contrast to Pt 4f in Pt/C (Pt $4f_{5/2}$ 75.05 eV), Pt 4f in TiN@Pt Ns (Pt $4f_{5/2}$, 74.43 eV) shifted negatively, demonstrating that the Pt thin layer of TiN@Pt acquired electrons from TiN Ns. This can further result in a downward-shift of the d band center for Pt, weakened OH* species binding energy, and improved ORR performance (Fig. 12f) for TiN@Pt Ns. As shown in Fig. 12g, TiN@Pt Ns possesses a well MA of 0.44 mA g_{Pt}^{-1} and specific activity of 0.33 mA cm^{-2} (at 0.9 V *vs.* RHE). The prepared catalysts outperform commercial Pt/C catalysts in identical test conditions, maintaining a high level of activity (61% of the initial value) after 3000 consecutive cycles (Fig. 12h). This study offers a framework for the development of low-Pt loading, long-lasting non-carbon catalysts.[127]

Stevens *et al.* prepared MoN thin films *via* the DC reactive sputtering. In this work, the *in situ* compositional and morphological changes of MoN thin films (Fig. 12a–c) were investigated by changing the applied potential in acid. At higher potentials (≥0.8 V *vs.* RHE), the film incorporates O, dissolved and roughened, suggesting that the enhancements in the performance can be due to the more accessible active sites. DFT and Pourbaix analysis further verified the high potential-induced film stability. Therefore, this report provided an approach for studying nontraditional surfaces by a rational and *in situ* tuning of the active sites to improve their performance.[128]

3.3.3 Modified transition metal nitride carriers. In order to increase the active surface area and the current density, nonmetallic elements (*e.g.*, O and P) and metallic elements (*e.g.*, Co, Ni, and Zr) were doped into metal nitrides to synthesize polyphase or single-phase metal nitrogen oxides and bimetallic nitrides, which replaced carbon carriers as new ORR carriers or platinum-free catalysts. Chisaka *et al.* synthesized carbon-free TiO_xN_y catalysts for PEMFC cathodes by a solution-phase combustion route. The TEM image (Fig. 13a) and XRD patterns demonstrate the formation of TiO_xN_y catalysts. Compared with the previously reported TiO_xN_y–C, TiO_xN_y increased the activity in the half-cell to be close to that of commercial Pt/C (Fig. 13b and c).[129] Subsequently, in order to

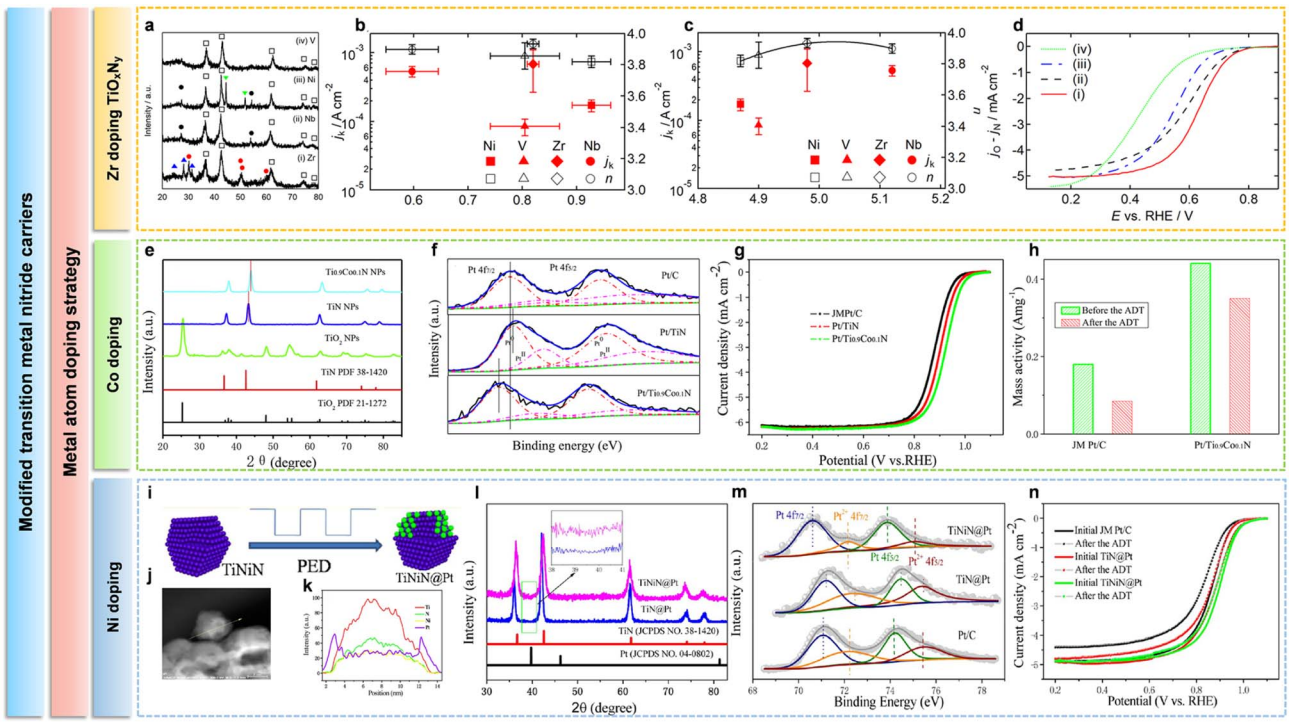

Fig. 14 (a) XRD patterns of the four metal-doped titanium oxynitride ($Ti_{0.8}M_{0.2}O_xN_y$) catalysts, where M = (i) Zr, (ii) Nb, (iii) Ni, and (iv) V. (b) Kinetic current density and number of electrons transferred per unit oxygen molecules *versus* the nitrogen doping level in oxide surface curves (j_k–*y* and *n*–*y* curves, respectively). (c) j_k and *n versus* the work function, *Φ*, curves. (d) RDE voltammograms of $Ti_{0.8}M_{0.2}O_xN_y$. Reproduced with permission.[134] Copyright 2022, The Royal Society of Chemistry. (e) XRD patterns of the prepared TiO_2, TiN, and $Ti_{0.9}Co_{0.1}N$ NPs. (f) XPS spectra of Pt 4f for Pt/C, Pt/TiN, and Pt/$Ti_{0.9}Co_{0.1}N$ catalysts. (g) The polarization curves of Pt/C and Pt/$Ti_{0.9}Co_{0.1}N$ catalysts in 0.1 M $HClO_4$ solution. (h) MA of Pt/C and Pt/$Ti_{0.9}Co_{0.1}N$, respectively. Reproduced with permission.[135] Copyright 2015, Elsevier B.V. (i) Synthetic route of TiNiN@Pt. (j) HAADF/STEM image of the TiNiN@Pt catalyst. (k) EDS line-scanning analysis along the yellow arrow marked in (j). (l) XRD patterns of TiN@Pt and TiNiN@Pt, inset: an enlargement of the boxed area. (m) Pt 4f XPS spectra and (n) polarization curves before and after the ADT test of Pt/C, TiN@Pt, and TiNiN@Pt, respectively. Reproduced with permission.[136] Copyright 2016, American Chemical Society.

identify the essential factors for enhancing the ORR activity in acidic media, Chisaka *et al.* investigated the active site generation process for carbon-support-free TiO_xN_y catalysts. It was discovered that the HCl concentration (c) in the precursor dispersion was crucial for the appearance of activity and improvement of surface nitrogen content. As c increased, the quantity of NH_4Cl also increased before pyrolysis; thus, after pyrolysis, the surface nitrogen level on the oxidized TiN also improved. Under optimal HCl concentration, the best carbon-supported oxide-based catalyst was nearly as active as the carbon-support-free TiO_xN_y (Fig. 13d).[130]

Despite TiN being well known as conductive carriers, the active oxidized surface of TiO_xN_y should have a lower conductivity than bulk TiN. Therefore, the enhancement of the surface electrical conductivity can promote the ORR activity. As reported, P^{5+} doping can be used to enhance the electron conductivity of anatase TiO_2.[133] Therefore, this approach may offer a potential economic and attractive chance to increase the ORR activity of TiO_xN_y with an amorphous or rutile TiO_2. Based on this, Chisaka *et al.* synthesized the novel P and N co-doped rutile TiO_2 ($TiO_xN_yP_z$) (Fig. 13e). This optimized new P^{5+}-derived active sites achieved the improvement of activity with a low catalyst loading (Fig. 13f). However, due to the partial depletion of both N and P atoms, the activity was not sufficiently stable after 5000 potential cycles between 1.0 and 1.5 V *vs.* RHE (Fig. 13g).[131]

A subsequent work used hypophosphorous acid as a phosphorus source to increase the surface phosphorus content on the disordered TiO_2 layer, which further enhanced the ORR activity (Fig. 13h). In acidic media, both the half-wave potential and limiting current density maximized to 0.66 V and 5.18 mA cm^{-2}, respectively (Fig. 13i). Besides, the stability against high potential cycles between 1.0 and 1.5 V (*vs.* RHE) was enhanced, which is critical to be used in vehicles. As shown in Fig. 13j, the reduction in half-wave potential during 5000 cycles was suppressed to 0.08 V, which is 0.03 V lower than that in a prior study while phosphoric acid was used as the P source.[132]

Metal-free atoms doping aside, transition metal atoms were likewise doped into TMNs to synthesize bimetallic nitrides. The synergistic effect between different metal atoms in bimetallic nitrides enhanced the electrochemical activity, which was conducive to enhance the electrochemical activity and stability. Therefore, Chisaka *et al.* also investigated the effect of foreign-metal doping on the ORR reactivity of TiN catalysts. After the doping of hetero-metal atoms, amorphous metal oxide layers were formed on the TiN surface, and the ORR selectivity was controlled by the work function of the resulting catalysts (Fig. 14a). Among them, Zr was demonstrated as the best catalyst to improve the ORR selectivity (Fig. 14d). This is due to the efficient electrons donated from the catalyst to O_2 molecules, and the work function can be adjusted to ~5.0 eV as well (Fig. 14b and c). Additionally, the Zr-doped TiN particles displayed a homogeneous and fine shape. All of these advantages are conducive to an improved ORR activity.[134]

Besides, Xiao *et al.* synthesized a innovative and durable non-carbon titanium cobalt nitride ($Ti_{0.9}Co_{0.1}N$), which was used as a carrier (Fig. 14e) for Pt in PEMFC cathode catalysts. The XPS measurements showed that the electronic transfer mechanisms of Co in $Ti_{0.9}Co_{0.1}N$ to Pt lowered the d-band center of the surface Pt atoms (Fig. 14f), which verified the SMSI between Pt NPs and $Ti_{0.9}Co_{0.1}N$. More importantly, compared to the commercial Pt/C electrocatalyst, $Ti_{0.9}Co_{0.1}N$-supported Pt catalyst ($Pt/Ti_{0.9}Co_{0.1}N$) demonstrated a significantly higher ORR activity (Fig. 14g) and durability (Fig. 14h) than that of the commercial Pt/C electrocatalyst.[135] Analogously, Tian *et al.* reported another novel catalyst with low Pt content, synthesized by placing several Pt atom layers on titanium nickel binary nitride (TiNiN) NPs (Fig. 14i–l). The XPS spectra of Pt 4f (Fig. 14m) demonstrated that Ni doping significantly increased the atomic ratio of Pt (0) in TiNiN@Pt, which further proved that the doping of Ni atoms contributed to enhance the SMSI between Pt and TiNiN. For the ORR in acid media, TiNiN@Pt exhibited an increased mass activity and specific activity by more than 400% and 200%, respectively, compared with the commercial Pt/C catalyst. Meanwhile, after 10 000 potential cycles, it displayed remarkable stability with barely any performance reduction (Fig. 14n).[136]

In conclusion, doping metal atoms serves the purpose of enhancing the MSI between TMNs and M (*e.g.*, Pt). As a concrete manifestation, active metal atoms gain more electrons from the carriers doped by metal atoms, resulting in a weakened interaction between intermediate oxide species and Pt atoms; hence, the ORR was activity improved. Meanwhile, the SMSI between M and TMNs is beneficial to stabilize the active metal atoms on the TMNs support.

3.4 Transition metal sulfide carriers (TMSs)

In addition to TMOs, TMCs, and TMNs, several studies have proved that transition metal sulfide (TMSs) are novel non-carbon carriers, especially the two-dimensional (2D) TMSs and Janus transition metal dichalcogenides (TMDs). This is due to their unique morphology, large specific surface area, adjustable electronic structure, tuned defect degree, *etc.*[137,138] To date, a series of TMSs–supported metal composites (TMSs–M*) has been reported for application in PEMFCs, including TMSs–supported metal nanoparticles, metal nanosheets, metal nanoclusters, and metal single atom.[139–141] Especially for the development of single atom catalysts (SACs), attention has been given toward designing ideal nanoscale supports for the anchoring of metal single atoms in PEMFC cathode catalysts, aiming to achieve the maximum atomic metal density and intrinsic properties of atomic metal active sites, clear structure–activity relationship, and remarkable ORR performance.[142–144]

3.4.1 MSI effect between TMSs and M*. As reported, unconventional phase 2D TMDs (1T′-2D TMDs) have a metallic character, which can make the nonbonding metal-d orbitals partially occupied. For the adsorption of single-metal atoms, it will result in a distinctive electrophilic characteristic,[139,145–147] resulting in the strong MSI in 2D TMDs-supported SACs. Besides, due to the single atomic layer/multiatomic layer structure, 2D TMDs have a large specific surface area and superior sensitivity to catalytic reaction intermediates. Although only the edge atoms of 2D TMDs structure retain the

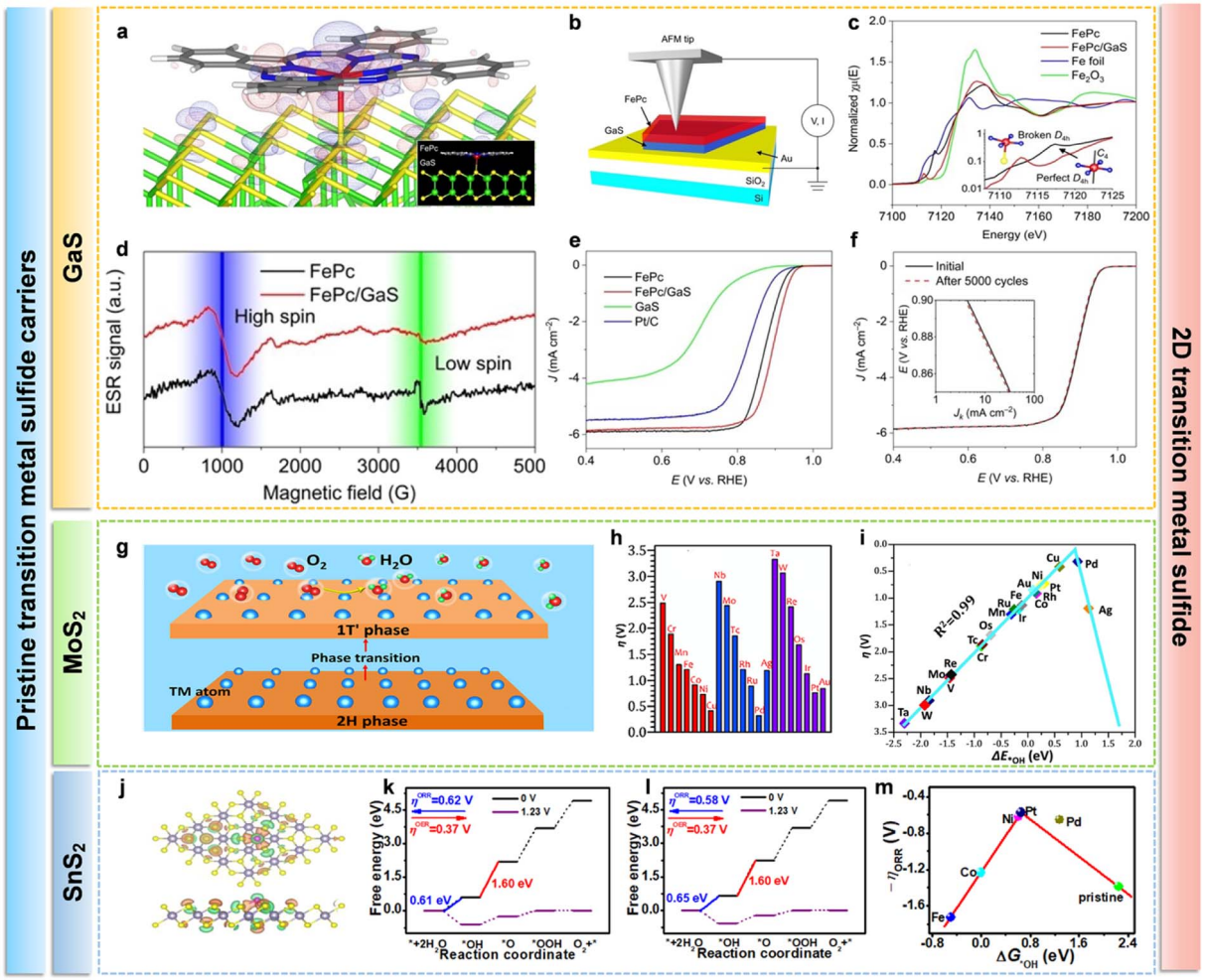

Fig. 15 (a) Plots of electron density difference. (b) Schematic illustration of the catalyst. (c) XANES spectra of Fe K-edge. Enlarged spectra in the pre-edge area are shown in the inset, along with matching schematic diagrams that highlight the symmetry of the FeN_4 molecule. (d) ESR spectra recorded at 100 K. (e) LSV curves of p–n junction catalyst. (f) LSV curves of FePc/GaS before and after 5000 potential cycles. Reproduced with permission.[150] Copyright 2022, Wiley-VCH GmbH. (g) Scheme of unconventional phase of the MoS_2 (1T′ phase). (h) Overview of the ORR overpotential for TM atoms supported on 1T′-MoS_2. (i) Scaling of overpotential and ΔE_{*OH} connection. Reproduced with permission.[140] Copyright 2021, American Chemical Society. (j) Charge density difference of TM/SnS_2. (k and l) Free energy diagram of (k) Ni, (l) Pt supported on the SnS_2 monolayer for the OER and ORR at $U = 0$ and 1.23 V. (m) ORR for pure and TM supported on SnS_2 monolayers with $-\eta^{ORR}$ *vs.* ΔG_{*OH}. Reproduced with permission.[138] Copyright 2022, American Chemical Society.

coordinatively unsaturated state, numerous in-plane atoms could activate and adsorb oxygen-containing intermediates by means of the modification strategy as well. Moreover, the metallic nature of 1T′-2D TMDs would also make for charging redistribution and carrier transport during the reaction process so as to further improve the catalytic efficiency.[140] Charge transfers between M* and the 2D TMDs monolayer could contribute to polarizing the surface, which will greatly enhance the active site of the reactants.[148,149] In addition, the intense interaction between the M* atoms and 2D TMDs monolayer surface implies the higher stability of M*, which prevents single atoms to aggregate into nanoparticles.[149] In conclusion, it is charge transfer and strong MSI between the carrier and M* that are beneficial for the catalytic activity of ORR.

3.4.2 Pristine transition metal sulfide carriers. As previously mentioned, at the atomic level, fine-regulating SACs to transcend their activity limitation remains challenging. Meanwhile, SACs with metal centers paired with nitrogen donors, such as iron phthalocyanine (FePc), possess p-type semiconductor properties, and a number of metal sulfides (*e.g.*, gallium sulfide (GaS)) have n-type semiconductor properties. Thus, Zhuang *et al.* proposed a novel strategy for generating charge transfer and strong interaction between metal and carriers (Fig. 15a and b). In brief, the local charge density of FePc (p-type semiconductor) is adjusted by GaS (n-type semiconductor) support with low work function, which leads to partial FeN_4 distortion (Fig. 15c) and spin state transition of the Fe^{II} center (Fig. 15d). As a result, FeN_4 SCAs supported by n-type GaS exhibited an excellent specific ORR activity (over twice and twelve times higher than that of pristine FePc and commercial Pt/C, respectively) at 0.85 V *vs.* RHE (Fig. 15e and f).[150]

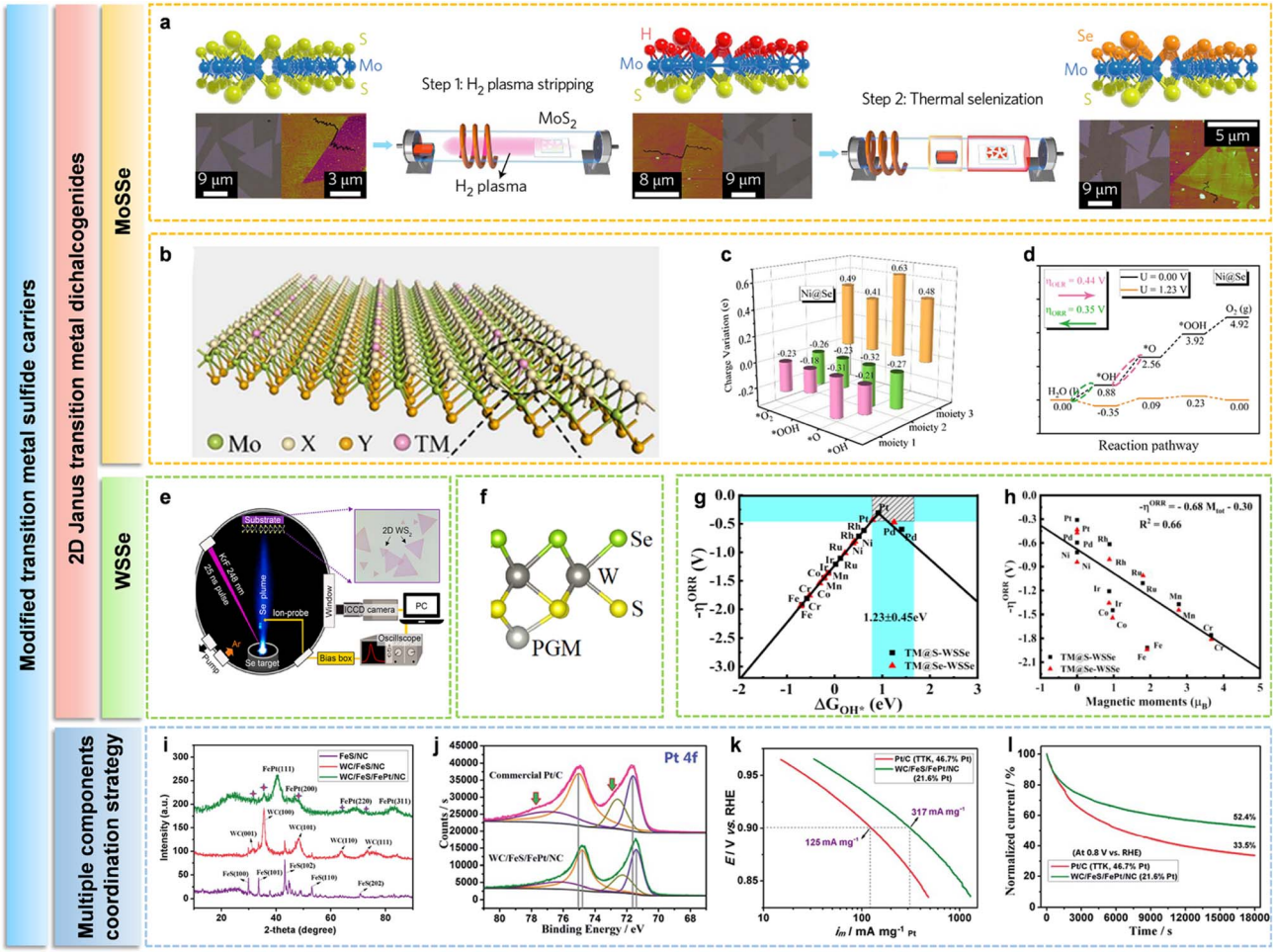

Fig. 16 (a) Synthesis illustration of 2D Janus MoSSe monolayer. Reproduced with permission.[156] Copyright 2017, Springer Nature. (b) Crystal structure of TM-doped Janus monolayer MoSSe. (c) Bader charge of the three moieties along the ORR procedure for Ni@Se. The anchored Ni, Janus MoSSe, and adsorbed species are represented by moieties 1–3 in (c), respectively. (d) Free energy diagrams during the ORR and OER processes of (c) Ni@Se. Reproduced with permission.[158] Copyright 2020, American Chemical Society. (e) The top-down method to engineer 2D WSSe monolayer. Reproduced with permission.[159] Copyright 2020, American Chemical Society. (f) Side view of single PGM (Ru, Rh, Pd, Os, Ir, Pt) atom supported on 2D Janus WSSe monolayer. Reproduced with permission.[160] Copyright 2022, Elsevier B.V. (g) Volcano plot for the opposite value of ORR overpotentials ($-\eta^{ORR}$) against ΔG_{OH*}. (h) The opposite value of $-\eta^{ORR}$ *vs.* the total magnetic moments of TM@S–WSSe and TM@Se–WSSe sites of WSSe monolayer. Reproduced with permission.[161] Copyright 2022, Elsevier B.V. (i) XRD patterns of the as-prepared samples. (j) Pt 4f XPS pattern of WC/FeS/NC and WC/FeS/FePt/NC samples. (k) ORR curves for various electrocatalysts. (l) Chronoamperometric curves for the electrocatalysts at 0.8 V under 1600 rpm. Reproduced with permission.[162] Copyright 2015, The Royal Society of Chemistry.

Besides, a series of 2D TMSs supports has been designed for the ORR process, such as MoS_2 and SnS_2. For example, Ling *et al.* demonstrated that as opposed to the traditional 2H phase, the defect-free MoS_2 monolayer in the unconventional phase (1T′-MoS_2) (Fig. 15g) can efficiently immobilize single TM atoms because of its unique electrophilic characteristic. Systematic first-principles calculations were performed to compare the ORR performance of 21 kinds of atomic TM sites@ 1T′-MoS_2. Two candidates, such as Cu and Pd@1T′-MoS_2, were successfully screened out with enhanced ORR properties (a low overpotential of 0.41 and 0.32 V respectively), exceeding the majority of the previously reported ORR catalysts (Fig. 15h). Furthermore, their potential for ORR were also revealed by comparing the adsorption energy (*OH) on different TM sites (Fig. 15i), which was determined by the d-band center of the supported TM sites.[140] This research provided efference to design stable and high-performance SACs for ORR. Yang *et al.* investigated the electrocatalytic oxygen evolution reaction (OER) and ORR performance of SnS_2 monolayer-supported transition metal (TM) atoms by DFT calculations (Fig. 15j). It is worthwhile to note that the OER/ORR overpotentials of Ni/SnS_2 and Pt/SnS_2 are 0.38/0.62 and 0.37/0.58 V, respectively, indicating promising catalytic performance (Fig. 15k and l). Moreover, compared with the contrast samples, SnS_2 monolayer-catalyst supported by Ni or Pt atoms showed the most potential application in OER/ORR (Fig. 15m). This research will pave the path toward the preparation of high-performance SnS_2-based bifunctional oxygen electrocatalysts and the application of PEMFC cathode catalysts in the future.[138]

3.4.3 Modified transition metal sulfide carriers. In addition, the novel 2D Janus TMDs monolayer materials (*e.g.*, MoSSe and WSSe) with asymmetric upper and lower surfaces have attracted quite a bit of attention and researches.[151–155] Lu *et al.* produced Janus MoSSe monolayer employing a self-regulating chemical vapour deposition device with an inductively linked plasma coil, breaking the out-of-plane structural symmetry (Fig. 16a).[156] Because the components on either side of the layer structure display distinct electronegativity, Janus MoSSe formations naturally possess a dipole moment. The simulation of the second-order magnetic susceptibility in-plane and out-of-plane of MoSSe monolayer exhibited anisotropy. Due to the unique characteristic of the Janus structures, holes and electrons can be effectively separated into distinct surfaces, which results in increased catalytic activity.[157]

On the basis of first-principles calculations, Wu *et al.* suggested Ni-doped Janus monolayer MoSSe (Fig. 16b) with superior electrocatalytic performance toward ORR for fuel cells. Fig. 16c showed the electrons transfer ability from the Ni atom and MoSSe to the reactant intermediates, and the Janus monolayer MoSSe doping Ni atoms by substituting Se atoms (Ni@Se) had the best electrons transfer ability among all the contrast samples. Meanwhile, Fig. 16d also verified the ultralow overpotential for ORR/OER. Additionally, the synergistic effects of the built-in electric field and heteroatom doping resulted in a high faradaic efficiency (about 100%) for ORR.[158] Guo *et al.* systematically explained the binding characteristics of single noble metal atoms (Pd, Pt, and Ir) anchored Janus MoSSe monolayers (MLs) by first-principles calculations. Additionally, the durability (Ir–MoSSe > Pt–MoSSe > Pd–MoSSe) as well as the binding and adjustable electronic properties were briefly investigated. As a result, Pd–MoSSe and Pt–MoSSe demonstrated outstanding bifunctional catalytic performance, especially the former having lower overpotentials (0.43 and 0.50 V for ORR and OER, respectively), which are better than the well-known Pt (111) (0.45 V) and IrO_2 (0.56 V) electrocatalysts. Therefore, Pd–MoSSe and Pt–MoSSe (especially the former) may act as promising extremely-efficient ORR/OER bifunctional electrocatalysts.[163]

Besides, Lin *et al.* proposed a new synthesis strategy for high-quality Janus WSSe ML by the precise tailoring of the hyperthermal property of pulsed laser ablation plasmas to implant Se species into WS_2 ML (Fig. 16e).[159] Guo *et al.* comprehensively investigated the PGM single atom-modified Janus WSSe monolayer systems by first-principles computations (Fig. 16f). The results displayed that the structural and electronic properties of Janus WSSe monolayer may be efficiently regulated by a single PGM atom sustained in a stable manner at the W top position on the S side. With the exceptional bifunctional catalytic activity elucidated, Pd–WSSe and Pt–WSSe are successfully screened from the PGM-WSSe systems. In particular, Pd–WSSe exhibits significantly lower overpotentials ($\eta_{ORR} \approx 0.39$ and $\eta_{OER} \approx 0.49$ V). Additionally, the superior electrical conductivity, high intrinsic electric field, moderate binding strength with O_2 molecule, and the d orbital occupancy of Pd and Pt atoms are the factors behind the remarkable bifunctional catalytic activity of Pd–WSSe and Pt–WSSe. As a result, it was possible to implement a successful technique to lower the PGM dosage in PGM SACs and an enhancement of the bifunctional catalytic performance of the Janus WSSe monolayer could be achieved.[160]

Similar to the above, Zhang *et al.* employed first-principles calculations to examine the ORR and OER electrocatalytic activity of Pt atoms anchored at the S and Se vacancy sites of the WSSe monolayer (Pt@S–WSSe, Pt@Se–WSSe). What's particularly different from previous researches[160,163] is that Pt@S–WSSe and Pt@Se–WSSe rather than WSSe monolayers anchored by Pd atoms have low ORR/OER overpotentials (η^{ORR}/η^{OER}) of 0.31/0.36 V and 0.43/0.34 V, respectively (Fig. 16g). Compared with the SACs previously researched, the η^{ORR} and η^{OER} of Pt@S–WSSe are much lower. In particular, it was demonstrated that TM@S–WSSe and TM@Se–WSSe exhibit close association between the magnetic moments and catalytic activities (Fig. 16h). The study above delivers novel perspectives for designing extremely effectual ORR and OER bifunctional SACs.[161]

Apart from single-component 2D Janus TMDs carriers, multicomponent catalysts containing metal sulfides provide a novel approach for the design of high-performance ORR electrocatalysts due to their high electrical conductivity, stability of supports, synergies between different components and the promoting effects on noble metals, which reveals broad application prospects in fuel cells. For instance, Li *et al.* proposed a novel hybrid material WC/FeS/FePt/NC (Fig. 16i). The Pt 4f XPS (Fig. 16j) spectra demonstrated that the WC/FeS/FePt/NC hybrid structure had a lower binding energy than Pt/C due to the incorporation of FeS, which indicated the electron donor from WC/FeS to Pt. As a consequence, WC/FeS/FePt/NC showed higher ORR activity (317 mA mg_{Pt}^{-1}) with MA 2.5 times that of Pt/C (125 mA mg_{Pt}^{-1}) at 0.9 V *vs.* RHE (Fig. 16k) and excellent stability in acidic electrolytes (Fig. 16l).[162]

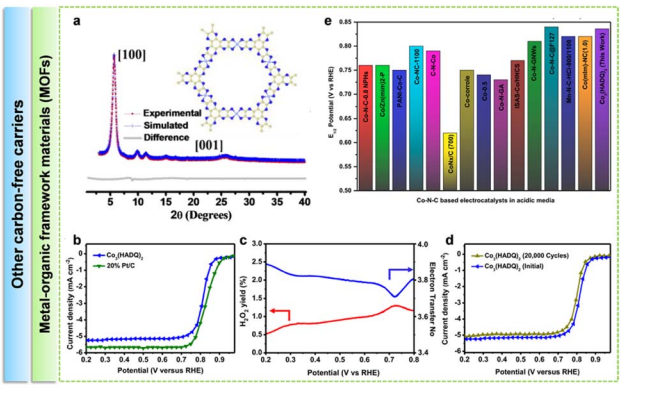

Fig. 17 (a) Powder XRD spectra of $Co_3(HADQ)_2$. (b) Linear scan voltammetry (LSV) curve of $Co_3(HADQ)_2$ and commercial 20% Pt/C at 1600 rpm. (c) H_2O_2 yield% of the ORR on $Co_3(HADQ)_2$ at 1600 rpm and electron transfer number utilizing RRDE for $Co_3(HADQ)_2$. (d) LSV curves for ORR prior to and following 20 000 cycles for the CV test at 1600 rpm. (e) Comparison of ORR activity ($E_{1/2}$) of different Co–N–C catalysts in acidic media in previously published literature. Reproduced with permission.[164] Copyright 2021, Elsevier B.V.

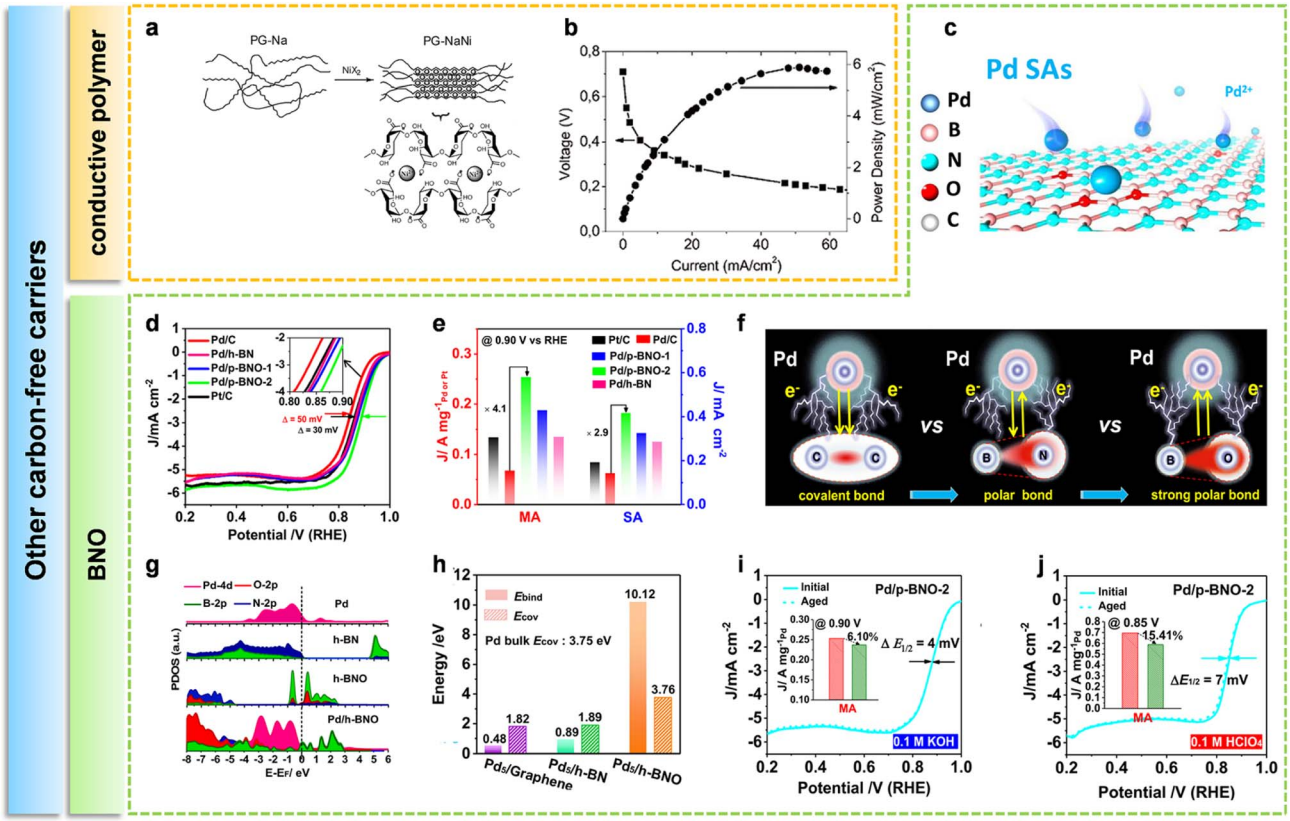

Fig. 18 (a) Scheme of the formation of polymer-complex structures. (b) Polarization and power density curves of the cathode and anode are PG-NaNi and Pt/C, respectively. Reproduced with permission.[176] Copyright 2018, The Royal Society of Chemistry. (c) Scheme of Pd/p-BNO. (d) ORR polarization curves of catalysts obtained in O_2-saturated 0.1 M KOH. (e) Comparisons in MA and surface activity at 0.90 V. (f) Design strategy to regulate the surface polarity of the support. (g) The PDOS of the d-state for Pd (with or without support) and the p-state for B, N, and O from the h-BN and h-BNO. (h) Binding energy between Pd and support as a function of the increasing SMSI effect, regulated by the polarity of the support. (i and j) ORR polarization curves and MA of Pd/p-BNO-2 before and after ADT (5000 CV cycles) in O_2-saturated 0.1 M KOH (i) and 0.1 M $HClO_4$ (j) solution. Reproduced with permission.[177] Copyright 2021, Elsevier B.V.

In conclusion, 2D TMSs and 2D Janus TMDs have received enormous attention in the field of electrocatalysts due to their unique crystal and band structures. At the same time, the excellent strength and stability of TMDs enable it to maintain its structure in harsh environments, ensuring the durability of the catalyst. As mentioned above, abundant studies have proved that 2D TMSs and 2D Janus TMDs has great application potential in the field of ORR by means of computational methods such as molecular dynamics and first principles. However, the experimental research of 2D Janus TMDs for ORR and the structure–activity relationship of 2D Janus TMDs as cathode catalyst carriers is still lacking, especially application in PEMFCs, which requires to be further explored.

3.5 Other carbon-free carriers

In addition to the above systems, metal–organic framework materials, oxygen-doped porous boron nitride (BNO), conductive polymer materials, and alloys can also be used as carriers for cathode catalysts for PEMFCs.

Functional porous frameworks, such as metal–organic frameworks (MOF)[165–169] and covalent organic frameworks (COFs),[170] have been used for energy storage and conversion devices due to their tunable porous interconnected structures, high specific surface areas, and well-dispersed active sites. Especially in the field of PEMFC, MOFs and their derivatives can be used as catalysts or ionomers for the construction of membrane electrode assembly (MEA) of PEMFCs.[171–174] For instance, Rashid *et al.* synthesized a new layer-stacked 2D MOF $Co_3(HADQ)_2$ (HADQ represents 2,3,6,7,10,11-hexaamine dipyrazino quinoxaline) for the first time (Fig. 17a), which demonstrated an extremely high activity ($E_{1/2}$ = 0.836 V *vs.* RHE, n = 3.93, and j_L = 5.31 mA cm^{-2}) with extraordinarily high conductivity of 8385.744 S m^{-1} (Fig. 17b and c) while exhibiting an outstanding stability (up to 20 000 cycles) as the electrocatalyst for ORR in an acidic media (pH = 0.29) (Fig. 17d), outperforming most of the state-of-the-art metal–N–C and single-atom electrocatalysts for acidic ORR (Fig. 17e).[164]

In addition, conductive polymer materials have also been widely used for PEMFCs due to their advantages of dimensional stability, thermal stability, conductivity, and flexibility, which can ultimately achieve the optimized interactions between M* and the polymer matrix and excellent PEMFCs properties.[175] Kadirov *et al.* synthesized a nickel sodium pectate complex (PG-NaNi) while nickel was substituted with sodium by 25% as the

cathode catalyst of PEMFCs, which is a readily available biological raw material and pectin (Fig. 18a). The values of the maximum current density was 59 mA cm^{-2} and the maximum power density was 5.9 mW cm^{-2} during tests in an H_2/O_2 PEMFC (Fig. 18b).[176] Li *et al.* discovered that the robust polar bond in the support can considerably boost the electrocatalytic oxygen reduction activity and durability of Pd NPs (Fig. 18c and d). The MA and surface activity of the optimized Pd/p-BNO are nearly 1.9 and 2.2 times higher than those of the commercial Pt/C catalyst under 0.90 V (*vs.*RHE), respectively (Fig. 18e). Through a combined experimental and computational investigation, it has been determined that the enhanced activity of Pd/p-BNO is due to the direct transfer of electrons *via* the strong polar O–B bonds from the support to the Pd NPs, which then results in the electron-rich Pd surface (Fig. 18f–h). Additionally, the stability of Pd/p-BNO is effectively increased by the strong bonding effect of the polar bond (Fig. 18i and j). This progress emphasizes the essential role of polar chemical bonds in carriers on inducing the SMSI effect, which may present new prospects for designing superior heterogeneous catalysts.[177]

As a novel multi-component catalyst, alloy nanoparticles could achieve high activity, high selectivity, and high stability through composition design and element regulation, which prompted them to be widely used in electrocatalysts for clean energy and possess broad application prospects in the field of electrocatalysis such as ORR.[178,179] Meanwhile, Pan *et al.* synthesized a novel alloy material FeCo in the amorphous phase with a highly porous structure, the merits of high-density defects and unsaturated surface atoms, which could be used as a bifunctional catalytic support to immobilize the Pd catalyst for high-performance ZAB.[180] Besides, Xia *et al.* demonstrated that the SMSI between Pt–Co alloys and Co–N_4 active sites reduced the adsorption energy of oxygen intermediates and the activation energy of the reaction, thereby synergically accounting for improving the ORR performance.[181]

4 Conclusions

PEMFCs have been regarded as one of the most eco-friendly and efficient devices to generate electricity. Yet the insufficient activity and stability of PEMFCs still hinders their widespread applications in different scenarios, which is mainly caused by the state-of-the-art Pt/C cathode catalysts. In particular, the negative problems brought by the utilization of carbon-based supports cannot be ignored. Recently, transition metals oxides, transition metal carbides, transition metal nitrides, and transition metal sulfides have been seen as alterative supports for carbon carriers. In this paper, we illustrated the up-to-date progress in carbon-free carriers for PEMFC cathode catalysts, focusing on their regulation strategies of MSI effect. To accomplish this obstacle, heteroatoms doping, coating engineering, forming heterostructures, and introducing oxygen vacancies and defect sites have been considered to be effective methods to prepare these carbon-free PEMFCs catalysts. Detailed researches by experimental and theoretical calculations have deepened our understanding of the MSI regulatory mechanism, where the adhesion energy, migration barrier, exposed crystal plane, d-band center, and electron transfer property of these carbon-free PEMFC cathode catalysts can be effectively tuned.

Several remaining challenges in carbon-free PEMFC cathode catalysts should be overcome in the future. The details are as follows.

(a) Conducting experimental research for application in PEMFCs to further illustrate the structure–activity relationship between metals and carbon-free carriers, especially TMSs. As for TMOs, TMCs, and TMNs, the existence of MSI is clearly characterized in combination with experimental researches and theoretical calculations; in addition, the structure–activity relationship of carbon-free cathode catalyst carriers and the acceleration of MSI effect on the ORR process in PEMFCs are gradually being illustrated. However, the experimental research of 2D Janus TMDs as cathode catalyst carriers for ORR and the MSI effect among them is still lacking, especially the application in PEMFCs, which requires to be further explored.

(b) Exploring effective methods to enhance the MSI and conductivity of carbon-free supports, which can further improve the ORR activity of non-carbon-supported PEMFC cathodes. Synthesizing carrier materials with heterojunction electronic regulation effect enhances the charge density of M*. For example, doping transition metal carbides and transition metal sulfides plays a vital role in enhancing the electrical conductivity; modifying hydroxyl groups (–OH) on the carrier surface is beneficial for improving the ability to anchor metal atoms; utilizing transition oxides with a more stable structure as the carrier skeleton could efficiently improve the durability of the catalyst in PEMFCs.

(c) The morphology and specific surface area of carbon-free supports are also need to be improved to prompt the anchoring of active metal sites and mass-transfer property of non-carbon supported PEMFC cathodes. Open frame structures such as nanotubes, nanoclusters, hollow mesoporous spheres, core–shell structures, multistage ordered pore structures, and two-dimensional structures (*e.g.*, MXenes) have attracted wide attention as electrocatalyst carriers due to their high surface exposure and atom utilization ratio, support-induced strain engineering, and adjustable electronic state.

(d) Design of novel carbon-free supports such as functional porous frameworks, composite non-carbon materials with heterojunction structures, molecular sieves porous carbon materials synthesized by means of a template agent such as SiO_2 with high porosity, specific surface area, and easy functionalization for PEMFCs, realizing the optimized O_2 adsorption, mass transfer, and electrochemical transformation.

(e) Machine learning has the prospects of accurately and reliably optimizing the experimental conditions by combining machine learning and DFT techniques to accomplish the accurate and reliable optimization of experimental conditions and developing novel models for PEMFC cathodes.

Given these challenges and issues, researchers need to further develop economical, eco-friendly, and highly durable carbon-free supported electrocatalysts to facilitate subsequent industrial applications of PEMFCs.

Author contributions

F.-L. D. conducted the literature search, writing, and creation of figures. Y.-R. L., Z.-H. L., C.-L. W., W.-X. Y., and B. W. supervised and revised the manuscript. All authors were involved in the discussion and critical revision and approved the final version of the manuscript.

Conflicts of interest

The authors declare no conflict of interest.

Acknowledgements

This work was financially supported by the National Key Research and Development Program of China (2020YFB1506300); National Natural Science Foundation of China (Grants No. 21971017, 21922502, 22075018 and 22375017); Young Elite Scientists Sponsorship Program by BAST (No. BYESS2023163); CNPC Innovation Found (2022DQ02-0606); Beijing Institute of Technology Research Fund Program.

References

1 J. Wang, X. Liu, L. Li, R. Liu, Y. Liu, C. Wang, Z. Lv, W. Yang, X. Feng and B. Wang, *Nano Res.*, 2023, **16**, 9327–9334.
2 W. Yang, X. Liu, H. Lv and J. Jia, *J. Colloid Interface Sci.*, 2021, **583**, 371–375.
3 X. Fei, W. Qi, X. Gui-Liang, Q. Xueping, H. Inhui, S. Cheng-Jun, L. Min, H. Wei, W. Hsi-wen, Z. Shangqian, L. Jin-Cheng, W. Jian-Gan, Z. Yuanmin, W. Duojie, W. Zidong, G. Meng, A. Khalil and S. Minhua, *Nat. Catal.*, 2022, **5**, 503–512.
4 Q. Qu, S. Ji, Y. Chen, D. Wang and Y. Li, *Trends Chem.*, 2021, **3**, 954–968.
5 Z. Zhao, Z. Liu, A. Zhang, X. Yan, W. Xue, B. Peng, H. L. Xin, X. Pan, X. Duan and Y. Huang, *Nat. Nanotechnol.*, 2022, **17**, 968–975.
6 S. Cherevko, N. Kulyk and K. J. J. Mayrhofer, *Nano Energy*, 2016, **29**, 275–298.
7 B. Huang, L. Bu, F. Ning, J. Zhou, C. Zhan, M. Sun, L. Li, Y. Zhu, Z. Hu, Q. Shao, X. Zhou and X. Huang, *Energy Environ. Sci.*, 2022, **15**, 3877–3890.
8 J. C. Meier, C. Galeano, I. Katsounaros, A. A. Topalov, A. Kostka, F. Schüth and K. J. J. Mayrhofer, *ACS Catal.*, 2012, **2**, 832–843.
9 J. Zhang, Y. Yuan, L. Gao, G. Zeng, M. Li and H. Huang, *Adv. Mater.*, 2021, **33**, 2006494.
10 C. A. Reiser, L. Bregoli, T. W. Patterson, J. S. Yi and T. D. Jarvi, *Electrochem. Solid-State Lett.*, 2005, **8**, A273–A276.
11 Z. Liu, H. Chen and T. Zhang, *Appl. Energy*, 2022, **327**, 120058.
12 H. Schulenburg, B. Schwanitz, N. Linse, G. G. Scherer, A. Wokaun, J. Krbanjevic, R. Grothausmann and I. Manke, *J. Phys. Chem. C*, 2011, **115**, 14236–14243.
13 J. Hong, M.-H. Jung, S. Cho, E.-B. Park, D. Yang, Y.-H. Kim, S.-H. Yang, W.-S. Jang, J. Jang, H. Lee, S. Lee, H. Jeong and Y.-M. Kim, *J. Energy Chem.*, 2022, **74**, 359–367.
14 Q. Ma, H. Jin, J. Zhu, Z. Li, H. Xu, B. Liu, Z. Zhang, J. Ma and S. Mu, *Adv. Sci.*, 2021, **8**, 2102209.
15 W. Yang, W. Zhang, R. Liu, F. Lv, Y. Chao, Z. Wang and S. Guo, *Chin. J. Catal.*, 2022, **43**, 110–115.
16 D. Xia, X. Yang, L. Xie, Y. Wei, W. Jiang, M. Dou, X. Li, J. Li, L. Gan and F. Kang, *Adv. Funct. Mater.*, 2019, **29**, 1906174.
17 X. Fu, F. M. Hassan, P. Zamani, G. Jiang, D. C. Higgins, J. Y. Choi, X. Wang, P. Xu, Y. Liu and Z. Chen, *Nano Energy*, 2017, **42**, 249–256.
18 T. Asset and P. Atanassov, *Joule*, 2019, **4**, 33–44.
19 L. Zong, K. Fan, W. Wu, L. Cui, L. Zhang, B. Johannessen, D. Qi, H. Yin, Y. Wang and P. Liu, *Adv. Funct. Mater.*, 2021, **31**, 2104864.
20 F. Lu, K. Fan and L. Cui, *Appl. Catal., B*, 2022, **313**, 121464.
21 Z. Qiao, C. Wang, C. Li, Y. Zeng, S. Hwang, B. Li, S. Karakalos, J. Park, A. J. Kropf, E. C. Wegener, Q. Gong, H. Xu, G. Wang, D. J. Myers, J. Xie, J. S. Spendelow and G. Wu, *Energy Environ. Sci.*, 2021, **14**, 4948–4960.
22 J. Wang, F. Pan, W. Chen, B. Li, D. Yang, P. Ming, X. Wei and C. Zhang, *Electrochem. Energy Rev.*, 2023, **6**, 6.
23 X. X. Wang, J. Sokolowski, H. Liu and G. Wu, *Chin. J. Catal.*, 2020, **41**, 739–755.
24 U. Martinez, S. Komini Babu, E. F. Holby, H. T. Chung, X. Yin and P. Zelenay, *Adv. Mater.*, 2019, **31**, 1806545.
25 C. X. Zhao, J. N. Liu, J. Wang, D. Ren, B. Q. Li and Q. Zhang, *Chem. Soc. Rev.*, 2021, **50**, 7745–7778.
26 L. Osmieri and Q. Meyer, *Curr. Opin. Electrochem.*, 2022, **31**, 100847.
27 X. F. Lu, B. Y. Xia, S. Q. Zang and X. Lou, *Angew. Chem., Int. Ed.*, 2019, **59**, 4634–4650.
28 Z. Li, B. Li, Y. Hu, X. Liao, H. Yu and C. Yu, *Small Struct.*, 2022, **3**, 2200041.
29 M. Tong, L. Wang and H. Fu, *Small Methods*, 2021, **5**, 2100865.
30 L. Yan, P. Li, Q. Zhu, A. Kumar, K. Sun, S. Tian and X. Sun, *Chem*, 2023, **9**, 280–342.
31 X. Liu, Y. Liu, W. Yang, X. Feng and B. Wang, *Chem. – Eur. J.*, 2022, **28**, e202201471.
32 C. Chen, M. Sun, K. Wang and Y. Li, *SmartMat*, 2022, **3**, 533–564.
33 P. Cui, L. Zhao, Y. Long, L. Dai and C. Hu, *Angew. Chem., Int. Ed.*, 2023, **62**, e202218269.
34 Z. Li, B. Li, Y. Hu, S. Wang and C. Yu, *Mater. Adv.*, 2022, **3**, 779–809.
35 X. Tian, X. F. Lu, B. Y. Xia and X. Lou, *Joule*, 2020, **4**, 45–68.
36 X. Huang, O. Akdim, M. Douthwaite, K. Wang, L. Zhao, R. J. Lewis, S. Pattisson, I. T. Daniel, P. J. Miedziak, G. Shaw, D. J. Morgan, S. M. Althahban, T. E. Davies, Q. He, F. Wang, J. Fu, D. Bethell, S. McIntosh, C. J. Kiely and G. J. Hutchings, *Nature*, 2022, **603**, 271–275.
37 Z. Luo, G. Zhao, H. Pan and W. Sun, *Adv. Energy Mater.*, 2022, **12**, 2201395.
38 X. Zhang, M. Zhang, Y. Deng, M. Xu, L. Artiglia, W. Wen, R. Gao, B. Chen, S. Yao, X. Zhang, M. Peng, J. Yan, A. Li,

Z. Jiang, X. Gao, S. Cao, C. Yang, A. J. Kropf, J. Shi, J. Xie, M. Bi, J. A. van Bokhoven, Y.-W. Li, X. Wen, M. Flytzani-Stephanopoulos, C. Shi, W. Zhou and D. Ma, *Nature*, 2021, **589**, 396–401.
39 X. Wan, Q. Liu, J. Liu, S. Liu, X. Liu, L. Zheng, J. Shang, R. Yu and J. Shui, *Nat. Commun.*, 2022, **13**, 2963.
40 C.-L. Yang, L.-N. Wang, P. Yin, J. Liu, M.-X. Chen, Q.-Q. Yan, Z.-S. Wang, S.-L. Xu, S.-Q. Chu, C. Cui, H. Ju, J. Zhu, Y. Lin, J. Shui and H.-W. Liang, *Science*, 2021, **374**, 459–464.
41 X. Zheng, P. Li, S. Dou, W. Sun, H. Pan, D. Wang and Y. Li, *Energy Environ. Sci.*, 2021, **14**, 2809–2858.
42 S. Y. Yao, X. Zhang, W. Zhou, R. Gao, W. Q. Xu, Y. F. Ye, L. L. Lin, X. D. Wen, P. Liu, B. B. Chen, E. Crumlin, J. H. Guo, Z. J. Zuo, W. Z. Li, J. L. Xie, L. Lu, C. J. Kiely, L. Gu, C. Shi, J. A. Rodriguez and D. Ma, *Science*, 2017, **357**, 389–393.
43 Z.-X. Sun, K. Sun, M.-L. Gao, Ö. Metin and H.-L. Jiang, *Angew. Chem., Int. Ed.*, 2022, **61**, e202206108.
44 T. Pu, W. Zhang and M. Zhu, *Angew. Chem., Int. Ed.*, 2022, **62**, e202212278.
45 F. Ando, T. Gunji, T. Tanabe, I. Fukano, H. D. Abruña, J. Wu, T. Ohsaka and F. Matsumoto, *ACS Catal.*, 2021, **11**, 9317–9332.
46 F. B. Ometto, E. A. Carbonio, É. Teixeira-Neto and H. M. Villullas, *J. Mater. Chem. A*, 2018, **7**, 2075–2086.
47 Z. Zhang, J. Liu, J. Gu, L. Su and L. Cheng, *Energy Environ. Sci.*, 2014, **7**, 2535–2558.
48 X. Zheng, P. Li, S. Dou, W. Sun, H. Pan, D. Wang and Y. Li, *Energy Environ. Sci.*, 2021, **14**, 2809–2858.
49 M. Tang, S. Li, S. Chen, Y. Ou, M. Hiroaki, W. Yuan, B. Zhu, H. Yang, Y. Gao, Z. Zhang and Y. Wang, *Angew. Chem., Int. Ed.*, 2021, **60**, 22339–22344.
50 L. Yu, K. Sato, T. Toriyama, T. Yamamoto, S. Matsumura and K. Nagaoka, *Chem. – Eur. J.*, 2018, **24**, 8742–8746.
51 Y. Zhang, J. X. Liu, K. Qian, A. Jia, D. Li, L. Shi, J. Hu, J. Zhu and W. Huang, *Angew. Chem., Int. Ed.*, 2021, **60**, 12074–12081.
52 B. Han, Y. Guo, Y. Huang, W. Xi, J. Xu, J. Luo, H. Qi, Y. Ren, X. Liu, B. Qiao and T. Zhang, *Angew. Chem., Int. Ed.*, 2020, **59**, 11824–11829.
53 J. Zhang, J. Ma, T. S. Choksi, D. Zhou, S. Han, Y.-F. Liao, H. B. Yang, D. Liu, Z. Zeng, W. Liu, X. Sun, T. Zhang and B. Liu, *J. Am. Chem. Soc.*, 2022, **144**, 2255–2263.
54 Q. Ji, L. Bi, J. Zhang, H. Cao and X. S. Zhao, *Energy Environ. Sci.*, 2020, **13**, 1408–1428.
55 L. Castanheira, W. O. Silva, F. H. B. Lima, A. Crisci, L. Dubau and F. Maillard, *ACS Catal.*, 2015, **5**, 2184–2194.
56 F. Jiecai, J. Xiaolin, H. Weihua and C. Zhen, *Energy Storage Mater.*, 2021, **42**, 252–258.
57 X. Zhang, C. Feng, B. Dong, C. Liu and Y. Chai, *Adv. Mater.*, 2023, **35**, 2207066.
58 S. J. Tauster, S. C. Fung and R. L. Garten, *J. Am. Chem. Soc.*, 2002, **100**, 170–175.
59 S. Li, J. Liu, J. Liang, Z. Lin, X. Liu, Y. Chen, G. Lu, C. Wang, P. Wei, J. Han, Y. Huang, G. Wu and Q. Li, *Appl. Catal., B*, 2022, **320**, 122017.
60 Q. Lu, Z. Wang, Y. Tang, C. Huang, A. Zhang, F. Liu, X. Liu, B. Shan and R. Chen, *Sustainable Energy Fuels*, 2022, **6**, 2989–2995.
61 T. G. Mark, C. Lily, G. H. Michael, T. Wing-Man and L. Zheng-Hong, *Adv. Funct. Mater.*, 2012, **22**, 4557–4568.
62 M. T. Greiner, L. Chai, M. G. Helander, W.-M. Tang and Z.-H. Lu, *Adv. Funct. Mater.*, 2012, **23**, 215–226.
63 K. J. Rietwyk, D. A. Keller, A. Ginsburg, H. N. Barad, M. Priel, K. Majhi, Z. Yan, S. Tirosh, A. Y. Anderson, L. Ley and A. Zaban, *Adv. Mater. Interfaces*, 2019, **6**, 1802058.
64 T. C. Yeh, Q. Zhu, D. B. Buchholz, A. B. Martinson, R. P. H. Chang and T. O. Mason, *Appl. Surf. Sci.*, 2015, **330**, 405–410.
65 S. Hu and W.-X. Li, *Science*, 2021, **374**, 1360–1365.
66 M. Dou, M. Hou, Z. Li, F. Wang, D. Liang, Z. Shao and B. Yi, *J. Energy Chem.*, 2015, **24**, 39–44.
67 X. Li, X. I. Pereira-Hernández, Y. Chen, J. Xu, J. Zhao, C.-W. Pao, C.-Y. Fang, J. Zeng, Y. Wang, B. C. Gates and J. Liu, *Nature*, 2022, **611**, 284–288.
68 D. Kim, G. Dimitrakopoulos and B. Yildiz, *J. Am. Chem. Soc.*, 2022, **144**, 21926–21938.
69 L. Niu, R. Xu, Z. Jia, Y. Wang, Q. Xiao, H. Zhang and T. Qi, *Ionics*, 2021, **27**, 2571–2582.
70 C. He, X. Wang, S. Sankarasubramanian, A. Yadav, K. Bhattacharyya, X. Liang and V. Ramani, *ACS Appl. Energy Mater.*, 2020, **3**, 5774–5783.
71 P. Toan Minh, I. Kyungmin and K. Jinsoo, *Appl. Surf. Sci.*, 2022, **611**, 155740.
72 G. Shi, T. Tano, D. A. Tryk, A. Iiyama, M. Uchida and K. Kakinuma, *ACS Catal.*, 2021, **11**, 5222–5230.
73 H. Xie, X. Xie, G. Hu, V. Prabhakaran, S. Saha, L. Gonzalez-Lopez, A. H. Phakatkar, M. Hong, M. Wu, R. Shahbazian-Yassar, V. Ramani, M. I. Al-Sheikhly, D.-e. Jiang, Y. Shao and L. Hu, *Nat. Energy*, 2022, **7**, 281–289.
74 Y. Chen, X. Zheng, J. Cai, G. Zhao, B. Zhang, Z. Luo, G. Wang, H. Pan and W. Sun, *ACS Catal.*, 2022, **12**, 7406–7414.
75 J. Chang, G. Wang, M. Wang, Q. Wang, B. Li, H. Zhou, Y. Zhu, W. Zhang, M. Omer, N. Orlovskaya, Q. Ma, M. Gu, Z. Feng, G. Wang and Y. Yang, *Nat. Energy*, 2021, **6**, 1144–1153.
76 Z. Miao, S. Li, C. Priest, T. Wang, G. Wu and Q. Li, *Adv. Mater.*, 2022, **34**, 2200595.
77 S. Kumari and P. Sautet, *J. Mater. Chem. A*, 2021, **9**, 15724–15733.
78 M. Li, H. Liu, T. Lv and M. Ding, *J. Mater. Chem. A*, 2018, **6**, 3488–3499.
79 Z. Lin, J. Liu, S. Li, J. Liang, X. Liu, L. Xie, G. Lu, J. Han, Y. Huang and Q. Li, *Adv. Funct. Mater.*, 2023, **33**, 2211638.
80 W. Li, D. Wang, Y. Zhang, L. Tao, T. Wang, Y. Zou, Y. Wang, R. Chen and S. Wang, *Adv. Mater.*, 2020, **32**, 1907879.
81 C. Chen, X.-T. Wang, J.-H. Zhong, J. Liu, G. I. N. Waterhouse and Z.-Q. Liu, *Angew. Chem., Int. Ed.*, 2021, **60**, 22043–22050.
82 S. R. Chemler and M. T. Bovino, *ACS Catal.*, 2013, **3**, 1184–1194.
83 R. B. Levy and M. Boudart, *Science*, 1973, **181**, 547–549.

84 M. A. Abdelkareem, T. Wilberforce, K. Elsaid, E. T. Sayed, E. A. M. Abdelghani and A. G. Olabi, *Int. J. Hydrogen Energy*, 2020, **46**, 23529–23547.
85 J. Sang Hoon and L. Jae Sung, *J. Catal.*, 2021, **404**, 911–924.
86 W. Yang, X. Liu, X. Yue, J. Jia and S. Guo, *J. Am. Chem. Soc.*, 2015, **137**, 1436–1439.
87 B. Hammer and J. K. Norskov, *Adv. Catal.*, 2000, **45**, 71–129.
88 J. R. Kitchin, J. K. Nørskov, M. A. Barteau and J. G. Chen, *Catal. Today*, 2005, **105**, 66–73.
89 B. M. Tackett, W. Sheng and J. G. Chen, *Joule*, 2017, **1**, 253–263.
90 Y. Wang, Q. Wu, B. Zhang, L. Tian and X. Zhang, *Catalysts*, 2020, **10**, 1164.
91 Y. Zhong, X. Xia, F. Shi, J. Zhan, J. Tu and H. J. Fan, *Adv. Sci.*, 2016, **3**, 1500286.
92 J. L. Bott-Neto, W. Beck, L. C. Varanda and E. A. Ticianelli, *Int. J. Hydrogen Energy*, 2017, **42**, 20677–20688.
93 A. M. Gómez-Marín, J. L. Bott-Neto, J. B. Souza, T. L. Silva, W. Beck, L. C. Varanda and E. A. Ticianelli, *ChemElectroChem*, 2016, **3**, 1570–1579.
94 Y. C. Kimmel, D. V. Esposito, R. W. Birkmire and J. G. Chen, *Int. J. Hydrogen Energy*, 2011, **37**, 3019–3024.
95 Z. Yan, G. He, M. Cai, H. Meng and P. K. Shen, *J. Power Sources*, 2013, **242**, 817–823.
96 Z. Li, L. Yu, C. Milligan, T. Ma, L. Zhou, Y. Cui, Z. Qi, N. Libretto, B. Xu, J. Luo, E. Shi, Z. Wu, H. Xin, W. N. Delgass, J. T. Miller and Y. Wu, *Nat. Commun.*, 2018, **9**, 5258.
97 Y. Lou, J. Xu, Y. Zhang, C. Pan, Y. Dong and Y. Zhu, *Mater. Today Nano*, 2020, **12**, 100093.
98 E. R. Hamo, R. Saporta and B. A. Rosen, *ACS Appl. Energy Mater.*, 2021, **4**, 2130–2137.
99 E. R. Hamo, R. K. Singh, J. C. Douglin, S. Chen, M. B. Hassine, E. Carbo-Argibay, S. Lu, H. Wang, P. J. Ferreira, B. A. Rosen and D. R. Dekel, *ACS Catal.*, 2021, **11**, 932–947.
100 D. V. Esposito, S. T. Hunt, Y. C. Kimmel and J. G. Chen, *J. Am. Chem. Soc.*, 2012, **134**, 3025–3033.
101 Y. C. Kimmel, X. Xu, W. Yu, X. Yang and J. G. Chen, *ACS Catal.*, 2014, **4**, 1558–1562.
102 C. Wan, Y. N. Regmi and B. M. Leonard, *Angew. Chem.*, 2014, **126**, 6407–6410.
103 C. He, S. Zhang and J. Tao, *ACS Appl. Energy Mater.*, 2022, **5**, 4382–4389.
104 A. M. Hofer, G. Mori, A. Fian, J. Winkler and C. Mitterer, *Thin Solid Films*, 2016, **599**, 1–6.
105 K. Lee, A. Ishihara, S. Mitsushima, N. Kamiya and K.-i. Ota, *Electrochim. Acta*, 2004, **49**, 3479–3485.
106 E. R. Hamo, P. Tereshchuk, M. Zysler, D. Zitoun, A. Natan and B. A. Rosen, *J. Electrochem. Soc.*, 2019, **166**, F1292–F1300.
107 E. R. Hamo and B. A. Rosen, *ChemElectroChem*, 2021, **8**, 3123–3134.
108 Y. Lee, J. H. Ahn, H.-Y. Park, J. Jung, Y. Jeon, D.-G. Lee, M.-H. Kim, E. Lee, C. Kim, Y. Kwon, H.-W. Lee, J. H. Jang, J. H. Lee and H.-K. Song, *Nano Energy*, 2020, **79**, 105363.
109 C. Eames and M. S. Islam, *J. Am. Chem. Soc.*, 2014, **136**, 16270–16276.
110 M. Naguib, O. Mashtalir, J. Carle, V. Presser, J. Lu, L. Hultman, Y. Gogotsi and M. W. Barsoum, *ACS Nano*, 2012, **6**, 1322–1331.
111 Y. Dai, B. Liu, Z. Zhang, P. Guo, C. Liu, Y. Zhang, L. Zhao and Z. Wang, *Adv. Mater.*, 2023, **35**, 221075.
112 K. Huang, Z. Li, J. Lin, G. Han and P. Huang, *Chem. Soc. Rev.*, 2018, **47**, 5109–5124.
113 A. Liu, X. Liang, X. Ren, W. Guan, M. Gao, Y. Yang, Q. Yang, L. Gao, Y. Li and T. Ma, *Adv. Funct. Mater.*, 2020, **30**, 2003437.
114 Q. Peng, J. Zhou, J. Chen, T. Zhang and Z. Sun, *J. Mater. Chem. A*, 2019, **7**, 26062–26070.
115 Y. Liu, X. Liu, Z. Lv, R. Liu, L. Li, J. Wang, W. Yang, X. Jiang, X. Feng and B. Wang, *Angew. Chem., Int. Ed.*, 2022, **134**, e202117617.
116 J. G. Chen, *Chem. Rev.*, 1996, **96**, 1477–1498.
117 J. Giner and L. Swette, *Nature*, 1966, **211**, 1291–1292.
118 H. Zhong, H. Zhang, Y. Liang, J. Zhang, M. Wang and X. Wang, *J. Power Sources*, 2007, **164**, 572–577.
119 H. Guan, W. Li, J. Han, W. Yi, H. Bai, Q. Kong and G. Xi, *Nat. Commun.*, 2021, **12**, 1376.
120 M. M. O. Thotiyl and S. Sampath, *Electrochim. Acta*, 2011, **56**, 3549–3554.
121 Y. Yue, P. Han, S. Dong, K. Zhang, C. Zhang, C. Shang and G. Cui, *Sci. Bull.*, 2012, **57**, 4111–4118.
122 D. Tian, S. R. Denny, K. Li, H. Wang, S. Kattel and J. G. Chen, *Chem. Soc. Rev.*, 2021, **50**, 12338–12376.
123 G.-T. Song, Y. Wang, Y. Qi, W.-M. Li and L.-X. Zhang, *Rare Met.*, 2019, **39**, 784–791.
124 T. Varga, G. Ballai, L. Vásárhelyi, H. Haspel, Á. Kukovecz and Z. Kónya, *Appl. Catal., B*, 2018, **237**, 826–834.
125 H. Wang, J. Li, K. Li, Y. Lin, J. Chen, L. Gao, V. Nicolosi, X. Xiao and J.-M. Lee, *Chem. Soc. Rev.*, 2020, **50**, 1354–1390.
126 R. Zeng, Y. Yang, X. Feng, H. Li, L. M. Gibbs, F. J. DiSalvo and H. D. Abruña, *Sci. Adv.*, 2022, **8**, eabj1584.
127 Z. Yuan, Y. Cao, Z. Zhang, Y. Fang, Q. Liu, D. Dang and Y. Zheng, *Int. J. Hydrogen Energy*, 2022, **47**, 15035–15043.
128 M. B. Stevens, M. E. Kreider, A. M. Patel, Z. Wang, Y. Liu, B. M. Gibbons, M. J. Statt, A. V. Ievlev, R. Sinclair, A. Mehta, R. C. Davis, J. K. Nørskov, A. Gallo, L. A. King and T. F. Jaramillo, *ACS Appl. Energy Mater.*, 2020, **3**, 12433–12446.
129 M. Chisaka, Y. Ando, Y. Yamamoto and N. Itagaki, *Electrochim. Acta*, 2016, **214**, 165–172.
130 M. Chisaka, Y. Yamamoto, N. Itagaki and Y. Hattori, *ACS Appl. Energy Mater.*, 2018, **1**, 211–219.
131 M. Chisaka and H. Morioka, *Catal. Sci. Technol.*, 2018, **9**, 611–619.
132 M. Chisaka, R. Xiang, S. Maruyama and H. Daiguji, *ACS Appl. Energy Mater.*, 2020, **3**, 9866–9876.
133 S. P. Madhusudanan, B. Gangaja, A. G. Shyla, A. S. Nair, S. V. Nair and D. Santhanagopalan, *ACS Sustain. Chem. Eng.*, 2017, **5**, 2393–2399.
134 M. Chisaka, T. Abe, R. Xiang, S. Maruyama and H. Daiguji, *Phys. Chem. Chem. Phys.*, 2022, **24**, 29328–29332.

135 Y. Xiao, G. Zhan, Z. Fu, Z. Pan, C. Xiao, S. Wu, C. Chen, G. Hu and Z. Wei, *J. Power Sources*, 2015, **284**, 296–304.
136 X. Tian, J. Luo, H. Nan, H. Zou, R. Chen, T. Shu, X. Li, Y. Li, H. Song, S. Liao and R. R. Adzic, *J. Am. Chem. Soc.*, 2016, **138**, 1575–1583.
137 Y. Wang, J. Mao, X. Meng, L. Yu, D. Deng and X. Bao, *Chem. Rev.*, 2018, **119**, 1806–1854.
138 F. Xia and F. Yang, *Energy Fuels*, 2022, **9**, 4992–4998.
139 Y.-C. Lin, D. O. Dumcenco, Y.-S. Huang and K. Suenaga, *Nat. Nanotechnol.*, 2014, **9**, 391–396.
140 F. Ling, W. Xia, L. Li, X. Zhou, X. Luo, Q. Bu, J. Huang, X. Liu, W. Kang and M. Zhou, *ACS Appl. Mater. Interfaces*, 2021, **13**, 17412–17419.
141 Q. Lu, H. Wu, X. Zheng, Y. Cao, J. Li, Y. Wang, H. Wang, C. Zhi, Y. Deng, X. Han and W. Hu, *Adv. Energy Mater.*, 2022, **12**, 2202215.
142 M. Tong, L. Wang and H. Fu, *Small Methods*, 2021, **5**, 2100865.
143 X. Xie, L. Shang, X. Xiong, R. Shi and T. Zhang, *Adv. Energy Mater.*, 2021, **12**, 2102688.
144 L. Zesheng, L. Bolin, H. Yifan, L. Xichun, Y. Huiqing and Y. Changlin, *Small Struct.*, 2022, **3**, 2200041.
145 M. Chhowalla, H. S. Shin, G. Eda, L.-J. Li, K. P. Loh and H. Zhang, *Nat. Chem.*, 2013, **5**, 263–275.
146 F. Ling, H. Jing, Y. Chen, W. Kang, W. Zeng, X. Liu, Y. Zhang, L. Fang and M. Zhou, *J. Mater. Chem. C*, 2018, **6**, 12245–12251.
147 H. Yang, S. W. Kim, M. Chhowalla and Y. H. Lee, *Nat. Phys.*, 2017, **13**, 931–937.
148 M. T. M. Koper, *J. Electroanal. Chem.*, 2011, **660**, 254–260.
149 X. Zhang, A. Chen, Z. Zhang, M. Jiao and Z. Zhou, *J. Mater. Chem. A*, 2018, **6**, 11446–11452.
150 Z. Zhuang, L. Xia, J. Huang, P. Zhu, Y. Li, C. Ye, M. Xia, R. Yu, Z. Lang, J. Zhu, L. Zheng, Y. Wang, T. Zhai, Y. Zhao, S. Wei, J. Li, D. Wang and Y. Li, *Angew. Chem., Int. Ed.*, 2022, **135**, e202212335.
151 X. Ma, X. Wu, H. Wang and Y. Wang, *J. Mater. Chem. A*, 2018, **6**, 2295–2301.
152 K. Ren, H. Qin, H. Liu, Y. Chen, X. Liu and G. Zhang, *Adv. Funct. Mater.*, 2022, **32**, 2110846.
153 D. B. Trivedi, G. Turgut, Y. Qin, M. Y. Sayyad, D. Hajra, M. Howell, L. Liu, S. Yang, N. H. Patoary, H. Li, M. M. Petrić, M. Meyer, M. Kremser, M. Barbone, G. Soavi, A. V. Stier, K. Müller, S. Yang, I. S. Esqueda, H. Zhuang, J. J. Finley and S. Tongay, *Adv. Mater.*, 2020, **32**, 2006320.
154 X. Wan, E. Chen, J. Yao, M. Gao, X. Miao, S. Wang, Y. Gu, S. Xiao, R. Zhan, K. Chen, Z. Chen, X. Zeng, X. Gu and J. Xu, *ACS Nano*, 2021, **15**, 20319–20331.
155 M. Yagmurcukardes, Y. Qin, S. Ozen, M. Sayyad, F. M. Peeters, S. Tongay and H. Sahin, *Appl. Phys. Rev.*, 2020, **7**, 011311.
156 A.-Y. Lu, H. Zhu, J. Xiao, C.-P. Chuu, Y. Han, M.-H. Chiu, C.-C. Cheng, C.-W. Yang, K.-H. Wei, Y. Yang, Y. Wang, D. Sokaras, D. Nordlund, P. Yang, D. A. Muller, M.-Y. Chou, X. Zhang and L.-J. Li, *Nat. Nanotechnol.*, 2017, **12**, 744–749.
157 Y. Ji, M. Yang, H. Lin, T. Hou, L. Wang, Y. Li and S.-T. Lee, *J. Phys. Chem. C*, 2018, **122**, 3123–3129.
158 Q. Wu, Y. Ma, H. Wang, S. Zhang, B. Huang and Y. Dai, *ACS Appl. Mater. Interfaces*, 2020, **12**, 24066–24073.
159 Y.-C. Lin, C. Liu, Y. Yu, E. Zarkadoula, M. Yoon, A. A. Puretzky, L. Liang, X. Kong, Y. Gu, A. Strasser, H. M. Meyer, M. Lorenz, M. F. Chisholm, I. N. Ivanov, C. M. Rouleau, G. Duscher, K. Xiao and D. B. Geohegan, *ACS Nano*, 2020, **14**, 3896–3906.
160 J.-X. Guo, S.-Y. Wu, G.-J. Zhang, S.-Y. Zhong and Z.-T. Wei, *Appl. Catal., A*, 2022, **643**, 118777.
161 X. Zhang, Z. Luo, Z. Zhou, Y. Wang, Z. Cui, Z. Gao, J. Shi, T. Cao and X. Fan, *J. Electroanal. Chem.*, 2022, **922**, 116731.
162 Z. Li, B. Li, Z. Liu, Z. Liu and D. Li, *RSC Adv.*, 2015, **5**, 106245–106251.
163 J.-X. Guo, S.-Y. Wu, G.-J. Zhang, L. Yan, J.-G. Hu and X.-Y. Li, *J. Colloid Interface Sci.*, 2022, **616**, 177–188.
164 I. Rashid, A. Sajjad, Y. Ghulam, I. Shumaila, T. Mohammad, H. Mathar, C. Henan, X. Hu, Z. Jie and Z. Wei, *Chem. Eng. J.*, 2021, **430**, 132642.
165 J. Li, W. Xia, J. Tang, Y. Gao, C. Jiang, Y. Jia, T. Chen, Z. Hou, R. Qi, D. Jiang, T. Asahi, X. Xu, T. Wang, J. He and Y. Yamauchi, *J. Am. Chem. Soc.*, 2022, **144**, 9280–9291.
166 L. Li, X. Liu, J. Wang, R. Liu, Y. Liu, C. L. Wang, W. Yang, X. Feng and B. Wang, *J. Mater. Chem. A*, 2022, **10**, 18723–18729.
167 J. Lv, W. Li, J. Li, Z. Zhu, A. Dong, H. Lv, P. Li and B. Wang, *Angew. Chem., Int. Ed.*, 2023, **62**, e202217958.
168 M. F. Sanad, A. R. Puente Santiago, S. A. Tolba, M. A. Ahsan, O. Fernandez-Delgado, M. Shawky Adly, E. M. Hashem, M. Mahrous Abodouh, M. S. El-Shall, S. T. Sreenivasan, N. K. Allam and L. Echegoyen, *J. Am. Chem. Soc.*, 2021, **143**, 4064–4073.
169 Z. Xinning, M. Xiaojie, Y. Yuqing, G. Caixia, X. Xiaojun, Z. Junwen and W. Bo, *Chem. Eng. J.*, 2022, **456**, 140939.
170 C. Wang, Z. Lv, W. Yang, X. Feng and B. Wang, *Chem. Soc. Rev.*, 2023, **52**, 1382–1427.
171 X. F. Lu, B. Y. Xia, S.-Q. Zang and X. W. D. Lou, *Angew. Chem., Int. Ed.*, 2019, **59**, 4634–4650.
172 X. X. Wang, D. A. Cullen, Y. T. Pan, S. Hwang, M. Wang, Z. Feng, J. Wang, M. H. Engelhard, H. Zhang, Y. He, Y. Shao, D. Su, K. L. More, J. S. Spendelow and G. Wu, *Adv. Mater.*, 2018, **30**, 1706758.
173 S. Yuan, J. Zhang, L. Hu, J. Li, S. Li, Y. Gao, Q. Zhang, L. Gu, W. Yang, X. Feng and B. Wang, *Angew. Chem., Int. Ed.*, 2021, **60**, 21685–21690.
174 Q. Zhang, S. Dong, P. Shao, Y. Zhu, Z. Mu, D. Sheng, T. Zhang, X. Jiang, R. Shao, Z. Ren, J. Xie, X. Feng and B. Wang, *Science*, 2022, **378**, 181–186.
175 G. Zhao, H. Zhao, X. Zhuang, L. Shi, B. Cheng, X. Xu and Y. Yin, *J. Mater. Chem. A*, 2020, **9**, 3729–3766.
176 M. K. Kadirov, S. T. Minzanova, I. R. Nizameev, L. G. Mironova, I. F. Gilmutdinov, M. N. Khrizanforov, K. V. Kholin, A. R. Khamatgalimov, V. A. Semyonov, V. I. Morozov, D. M. Kadirov, A. R. Mukhametzyanov, Y. H. Budnikova and O. G. Sinyashin, *Inorg. Chem. Front.*, 2018, **5**, 780–784.

177 Q. Li, X. Wang, Z. Xie, X. Peng, L. Guo, X. Yu, X. Yang, Z. Lu, X. Zhang and L. Li, *Appl. Catal., B*, 2021, **305**, 121020.
178 T. Shen, S. Wang, T. Zhao, Y. Hu and D. Wang, *Adv. Energy Mater.*, 2022, **12**, 2201823.
179 Z.-P. Wu, S. Shan, S.-Q. Zang and C.-J. Zhong, *Acc. Chem. Res.*, 2020, **53**, 2913–2924.
180 F. Pan, Z. Li, Z. Yang, Q. Ma, M. Wang, H. Wang, M. Olszta, G. Wang, Z. Feng, Y. Du and Y. Yang, *Adv. Energy Mater.*, 2020, **11**, 2002204.
181 S. Zaman, Y.-Q. Su, C.-L. Dong, R. Qi, L. Huang, Y. Qin, Y.-C. Huang, F.-M. Li, B. You, W. Guo, Q. Li, S. Ding and B. Xia, *Angew. Chem., Int. Ed.*, 2022, **61**, e202115835.